Self-assembly of aramid amphiphiles into ultra-stable nanoribbons and aligned nanoribbon threads

Self-assembly of aramid amphiphiles into ultra-stable nanoribbons and aligned nanoribbon threads

Ty Christoff-Tempesta[1], Yukio Cho[1], Dae-Yoon Kim[1§], Michela Geri[1], Guillaume Lamour[2], Andrew J. Lew[3], Xiaobing Zuo[4], William R. Lindemann[1], Julia H. Ortony[1]*

[1] Department of Materials Science and Engineering, Massachusetts Institute of Technology, Cambridge, MA 02139, USA

[2] Université Paris-Saclay, Univ Evry, CNRS, LAMBE, 91025, Evry-Courcouronnes, France

[3] Department of Chemistry, Massachusetts Institute of Technology, Cambridge, MA 02139, USA

[4] X-ray Science Division, Advanced Photon Source, Argonne National Laboratory, Argonne, IL 60439, USA

[§] Current Address: Institute of Advanced Composite Materials, Korea Institute of Science and Technology, Bondong, JB 55324, Korea

* Correspondence to: ortony@mit.edu

Abstract:

Small molecule self-assembly is an established route for producing high surface area nanostructures with readily customizable chemistries and precise molecular organization. However, these structures are fragile, exhibiting molecular exchange, migration, and rearrangement - among other dynamic instabilities - and ultimately disassociate upon drying. Here we show a small molecule platform, the aramid amphiphile (AA), that overcomes these dynamic instabilities by incorporating a Kevlar-inspired domain into the molecular structure. Strong, anisotropic interactions between AAs suppress molecular exchange and elicit spontaneous self-assembly in water to form nanoribbons with lengths of up to 20 microns. The nanoribbons have a Young's modulus of 1.7 GPa and tensile strength of 1.9 GPa. We exploit this stability to extend small molecule self-assembly to hierarchically ordered macroscopic materials outside of solvated environments. Through an aqueous shear alignment process, we organize AA nanoribbons into arbitrarily long flexible threads that support 200 times their weight when dried. Tensile tests of the threads provide a benchmark for Young's moduli (between ~400 and 600 MPa) and extensibilities (between ~0.6 and 1.1%) that depend on the counterion chemistry in solution. This bottom-up approach to macroscopic materials could benefit solid-state applications, historically inaccessible by self-assembled nanomaterials.

Spontaneous self-assembly of small amphiphilic molecules in water provides a powerful route to nanoscale structures with molecular-scale dimensions and pristine internal organization[1,2]. High-aspect-ratio nanostructures afforded by molecular self-assembly may be entangled or aligned, while maintaining high surface areas and tunable surface chemistries[3,4]. However, these supramolecular structures are generally fragile due to their weak intermolecular interactions[5,6] and pervasive dynamic instabilities – i.e. molecular exchange, migration, insertions, rearrangements, and transpositions[7-9]. Further, internal transient water contributes to the vulnerability of amphiphilic nanostructures by facilitating enzymatic or hydrolytic degradation[10,11]. Because of these limitations, small molecule assemblies are generally developed for biomaterials applications, where fast dynamics and biodegradability are harnessed as key design features[12-14]. These properties preclude their use in air, where they lack the structural stability imposed via the hydrophobic effect that is required to hold them together. Therefore, an amphiphile self-assembly platform that minimizes dynamics is an important target and could provide an approach to solid-state applications for which precise molecular organization, nanoscale structure, tunable surface chemistries, and water-processability are desirable[15]. Such solid-state applications could range from ion transporting to thermally conductive soft materials[16,17].

A reliable strategy for enhancing mechanical properties of molecular materials is to incorporate hydrogen bonding domains into the molecular design[18]. For example, the collective hydrogen bonding between aromatic amides (aramids) in Kevlar (poly(*p*-phenylene terephthalamide), PPTA) lead to its renowned strength and impact resistance[19]. Similar aramid chemical motifs have been incorporated into the design of biomimetic peptide-based amphiphiles[20,21]; however, in these cases, the impact of the aramid domains on mechanical properties remains unknown. In contrast to small amphiphilic molecules, polymeric aramid nanofibres composed of PPTA have shown strong mechanical behavior[22], even upon drying, but neither control over nanofibre surface chemistry nor precise internal molecular organization is achievable. In a handful of cases, molecules containing aramid moieties have aggregated in a variety of solvents into short rod-like or hockey-puck micelles, with the longest dimension on the order of tens or

hundreds of nanometers.[23-25] Despite these contributions, rational design of amphiphiles to form mechanically robust high-aspect-ratio nanostructures and the processing of these nanostructures into aligned solid-state 1-dimensional materials remains an important goal.

Here we show a molecular design motif that incorporates aramids as a structural domain within small molecule amphiphiles. This design produces aramid amphiphiles (AAs), molecules that self-assemble in water to form nanoribbons. AA nanoribbons are designed to be intrinsically hydrolysis-resistant, containing amides that are buried in the hydrophobic interior of the nanostructure, away from water[10]. AAs incorporate three attributes to suppress exchange dynamics and to enhance mechanical properties: (1) a high hydrogen bond density, with six hydrogen bonds per molecule; (2) in-register organization within each hydrogen bond network and the ability to form interplane π-π stacking[26]; and (3) minimal steric packing strain and torsion to minimize hydrogen bond distances[27], achieved by incorporating unobtrusive amphiphile head and tail groups into the molecular design. As a result, these nanoribbons are candidates for alignment and removal from water while maintaining their structure to obtain macroscopic, air-stable threads.

Self-assembled nanoribbons with suppressed exchange dynamics

We synthesized AAs with three different head group chemistries to tune the surface charge of the nanoribbons (Figure 1a): compound **1**, an anionic pentetic acid amphiphile, compound **2**, a zwitterionic ammonium sulfonate amphiphile, and compound **3**, a cationic triazaheptane amphiphile (Supplementary Schemes S1-S3, Supplementary Figs. 1-16). The structural domains of compounds **1**-**3** contain three aramid repeat units, and the hydrophobic tails consist of branched, six-carbon neopentyl groups. These features are designed to elicit spontaneous self-assembly in water into nanostructures with strong intermolecular interactions (Figure 1b).

We observe the assembly of **1**, **2**, and **3** in water into high-aspect-ratio nanoribbons by conventional transmission electron microscopy (TEM) (Figure 1c, Supplementary Fig. S21). The nanostructures' stability and high-aspect-ratios allow for shear alignment during gelation. This process leads to arbitrarily long threads (Figure 1d) that remain intact when removed from water (Figure 1e).

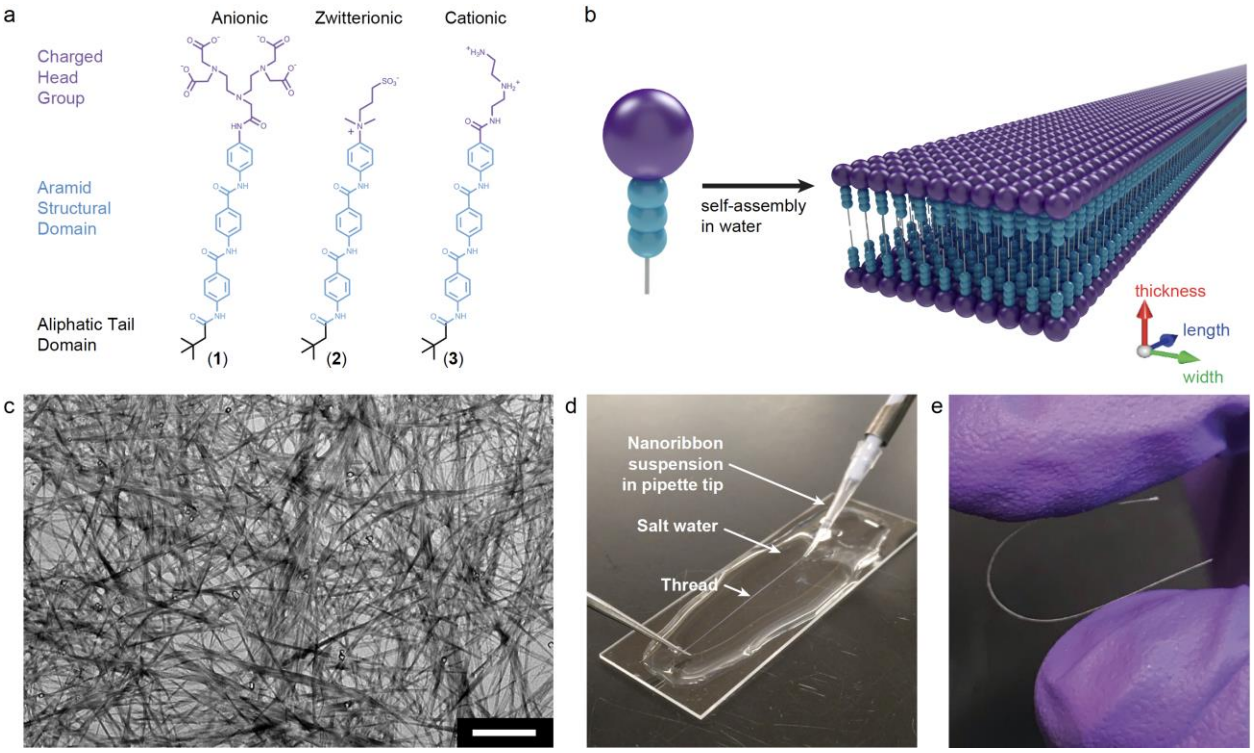

Figure 1. Kevlar-inspired aramid amphiphiles self-assemble into ultra-stable nanoribbons capable of hierarchical ordering to form dry macroscopic threads. a, Aramid amphiphiles are composed of a charged head group and an aliphatic tail to induce amphiphilic self-assembly, and an aramid structural domain to yield collective intermolecular hydrogen bonding. Aramid amphiphiles **1**, **2**, and **3** have anionic, zwitterionic, and cationic head groups, respectively. **b**, Aramid amphiphiles are designed to spontaneously self-assemble in water into nanoribbons with suppressed exchange dynamics. **c**, Dried nanoribbons of **2** are observed in a representative transmission electron micrograph (TEM) (scale bar, 1 μm). **d**, A nanoribbon suspension (compound **3**) is pulled out of a pipet tip by tweezers into a sodium sulfate solution to form a 1-dimensional gel. **e,** The gel is removed from water and dried to form a thread composed of aligned nanoribbons that can be bent and handled easily.

Small angle X-ray scattering (SAXS) profiles of compounds **1-3** in water fit most closely to a lamellar bilayer model (Figure 2a, Supplementary Fig. 25).[28,29] This fit gives a nanoribbon thickness of 3.9 nm for **1**, **2**, and **3**, which is corroborated by atomic force microscopy (AFM) height profiles

(Supplementary Fig. 28). The observed slope of -2 in the low-*q* regime of the SAXS profiles further suggests one-dimensional nanostructures in solution.[30] Cryogenic TEM (cryo-TEM) was used to image the nanoribbons in water at higher resolution for determining nanoribbon widths. Based on cryo-TEM, the widths of nanoribbons of **1**, **2**, and **3** are 5.5 nm, 5.1 nm, and 5.8 nm, respectively (Figure 2b, Supplementary Fig. 23). We find that the nanoribbon geometry is insensitive to temperature and concentration, where nanoribbons of **3** are observed up to 80 °C and from 0.1 to 20 mg/mL, but sensitive to pH (Supplementary Fig. S22, S26). Interestingly, we observe that self-assembled AA nanoribbons elongate upon bath sonication (with powers of approximately 10 mW/mL), reaching extraordinary lengths of up to 20 μm,[31,32] corresponding to width-to-length aspect-ratios of 4,000:1. Sonication has been previously shown to facilitate reorganization of hydrogen bonding in self-assembling systems[33]. The observed high-aspect-ratios of AA nanoribbons confirm that highly anisotropic intermolecular interactions occur between the nanoribbon long and wide axes (Supplementary Figs. 21, 28).

The nanoribbon geometry allows us to draw conclusions about the molecular packing. We observe through AFM height profiles a nanoribbon thickness approximately equal to two molecular lengths. Knowing that the hydrophilic head group must be exposed to water and the hydrophobic region (including the structural domain) must be shielded, we deduce that interdigitation between the molecules in the assembly must be limited to their short aliphatic tails. Concomitantly, we conclude that the molecules most likely adopt lamellar packing, which is corroborated by fits of SAXS profiles to a lamellar model (Figure 2a, Supplementary Section S3c). This molecular arrangement deviates from the 2-dimensional networks observed in solid-state crystals of oligomeric *p*-benzamide crystals[34,35] since the driving force for amphiphilic self-assembly imposes orientational constraints that differ from those implicated in crystallization[36].

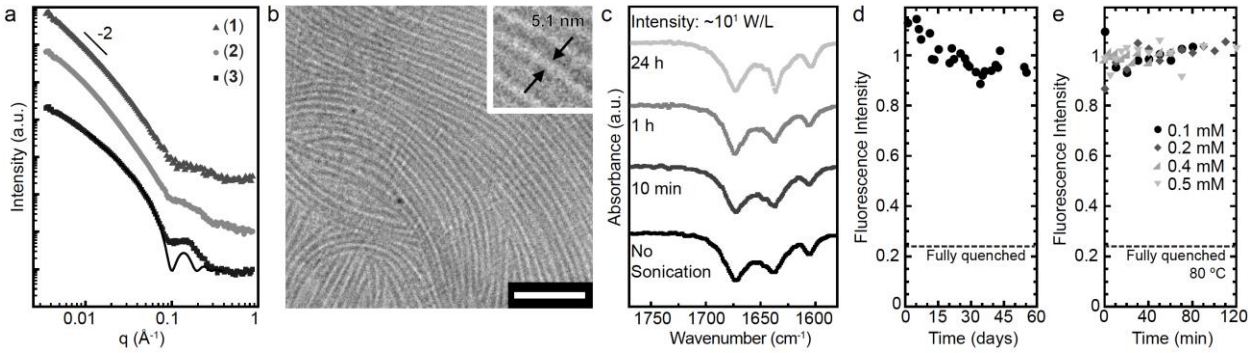

Figure 2. Aramid amphiphile nanoribbons exhibit minimal molecular exchange. a, Small angle X-ray scattering of **1**, **2**, and **3** nanoribbons in water shows a slope of -2 in the low-*q* regime, indicating high-aspect-ratio structures, and is best fit to a lamellar model (black line) giving a 3.9 nm nanoribbon thickness, consistent with nanoribbon geometries. **b**, Representative cryogenic TEM of nanoribbons of **2** in water reveals nanoribbon widths of approx. 5 nm (scale bar, 100 nm). **c**, ATR-FTIR of compound **3** nanoribbons shows the emergence of a sharp peak at 1638 cm^{-1} upon bath sonication, consistent with strengthening of the hydrogen bond network. **d**, Normalized fluorescence intensities of a 1:1 mixture of donor- and quencher-labeled nanoribbon suspensions are measured over 55 days. A nearly constant fluorescence intensity indicates minimal dark quenching and corresponds to minimal molecular exchange between nanoribbons over this time period. As a control, complete co-assembly of donor and quencher amphiphiles result in a 76% decrease in fluorescence intensity, illustrated by the horizontal dotted line (Supplementary Section S3f). **e**, Normalized fluorescence intensities of mixtures of donor- and quencher-labeled nanoribbon suspensions at 80 °C show that FRET dark quenching is not observed upon heating. This experiment was carried out with AA concentrations ranging from 0.1 to 0.5 mM, and no changes in exchange were observed.

We performed attenuated total reflectance Fourier-transform infrared spectroscopy (ATR-FTIR) on solutions of compound **3** as a function of bath sonication time to observe the evolution of hydrogen bonding with nanoribbon formation in solution. Compound **3** nanoribbons are selected for this analysis because their solubility is high, and consequently produce the strongest signal of compounds **1**-**3**. However, molecular packing is likely dominated by the aramid structural domain, which is equivalent in all three AA compounds. Therefore, we expect the molecular packing of compound **3** to be representative of all AA nanoribbons, **1**-**3**, particularly because they all exhibit similar nanoribbon geometries. Shown in Figure 2c, a peak at 1638 cm^{-1}, corresponding to a carbonyl (C=O) amide I stretch and characteristic of β-sheet hydrogen bonding, becomes more pronounced as sonication time increases. The sharpening of this peak indicates that uniformity of intermolecular hydrogen bonding distances increases upon sonication, likely because sonication provides the necessary energy to overcome kinetic traps. As a control, addition

of a denaturant, DMSO, to the nanoribbon suspension results in a suppression of the amide I peak, consistent with disruption of the hydrogen bonding network (Supplementary Fig. 20). The peaks at 1672 cm^{-1} and 1600 cm^{-1} are assigned to carbonyl stretching of the amide bond connecting the head group to the aramid structural domain and carbon-carbon stretching in the aromatic units, respectively, and their positions and intensities are therefore less sensitive to molecular packing (Supplementary Fig. 19)[37,38].

Collective hydrogen bonding within AA nanoribbons is expected to lead to strong internal cohesion and therefore slow molecular exchange dynamics[6]. We probed the rate at which individual AA molecules exchange between adjacent nanoribbons by Förster resonant energy transfer (FRET) dark quenching (Supplementary Section S3f)[39]. We mixed separate nanoribbon suspensions containing either fluorophore- or quencher-tagged amphiphiles and observed minimal molecular exchange between adjacent nanoribbons over 55 days (Figure 2d). Further, no changes in peak fluorescence intensity were observed when mixtures of fluorophore- and quencher-labeled nanoribbons were heated to 80 °C over a range of concentrations (Figure 2e). These results highlight the stability that aramid hydrogen bonding imparts on amphiphilic nanoribbon assemblies, representing a substantial departure from the typical exchange rates of 1-2 hours reported in phospholipid membranes and supramolecular peptide assemblies[8,9]. The slow exchange dynamics of AA nanoribbons allow us to perform single-nanoribbon mechanical characterization experiments.

Mechanical properties of individual nanoribbons

Direct mechanical characterization of solid-state nanofibres has previously been demonstrated to yield stress-strain profiles via AFM force measurements.[40,41] However, this method requires that the widths of the fibres are large relative to the radius of curvature of the AFM tip. In the case of small nanostructures whose widths are less than 10 nm, as observed in AA nanoribbons, direct mechanical measurements pose significant experimental challenges. To circumvent the lower bound size limitation, indirect methods of nanofibre mechanical characterization have been developed[42-44]. These methods are based on AFM imaging of nanofilaments or nanofilament fragments followed by statistical analyses to

determine Young's moduli or tensile strengths. Such studies have uncovered mechanical properties of a range of nanofilaments with diameters on the order of 10 nm including silver nanowires, carbon nanotubes, and amyloid fibrils[42,44,45].

We characterized the Young's modulus of AA nanoribbons using statistical topographical analysis of AFM images. The Young's modulus of compound **3** nanoribbons was measured due to its high solubility and for consistency among characterization techniques. Mechanical properties arise from the region with the strongest intermolecular interactions – the aramid structural domain – so we expect nanoribbons of **1** and **2** to exhibit similar Young's moduli and tensile strengths as compound **3**. The shape fluctuations of compound **3** nanoribbons (n = 29) in water equilibrated on a glass surface were used to determine their bending rigidity (Figure 2d)[42,43]. Parametric splines to the contours of each nanoribbon were traced (Figure 3a) and fit to determine a persistence length, P = 3.9 ± 0.7 μm, from which the Young's modulus was calculated to be E = 1.7 ± 0.7 GPa (Figure 3b, Supplementary Section S3g).

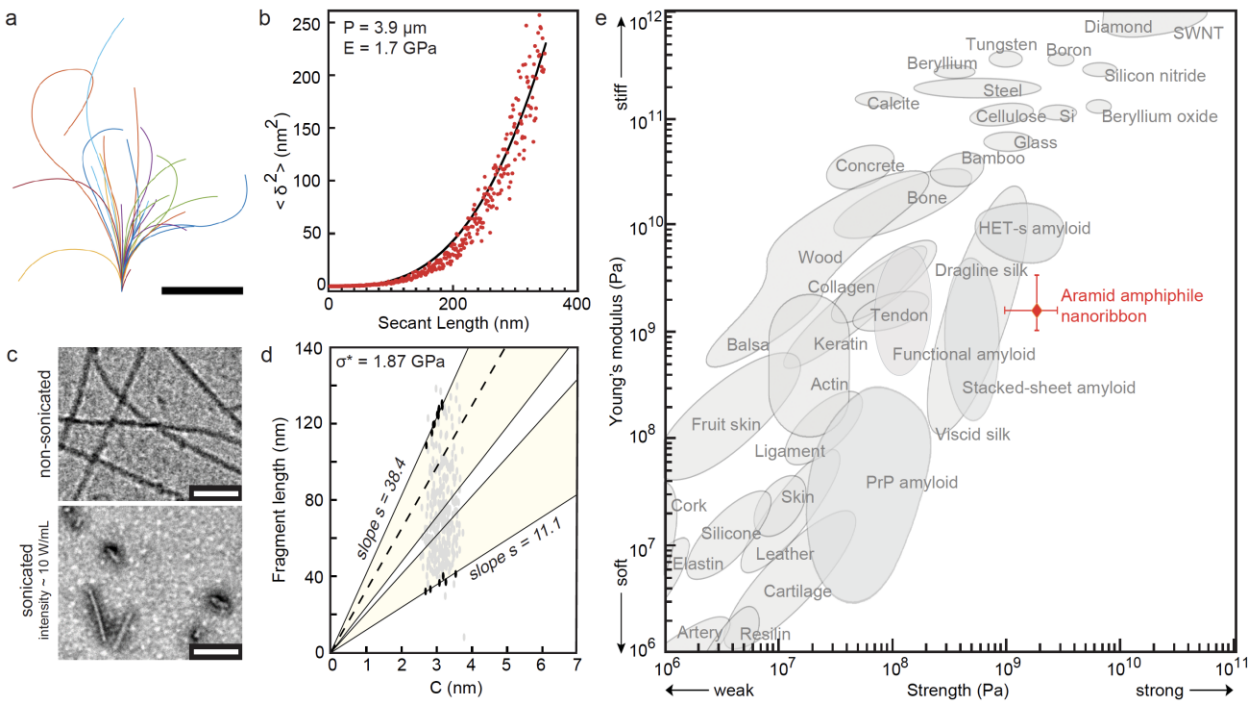

Figure 3. Aramid amphiphile nanoribbons have a Young's modulus of E = 1.7 GPa, and a tensile strength of σ* = 1.9 GPa. a, Contours acquired by tracing the AFM profiles of 29 AA nanoribbons are used for statistical topographical analysis (scale bar, 1 μm). **b**, Midpoint deviations δ from contour traces are used to calculate a persistence length, P = 3.9 ± 0.7 μm and Young's modulus, E = 1.7 ± 0.7 GPa, from least-squares fitting of a worm-like chain model for semi-flexible polymers to the data. **c**, Sonication-induced scission of nanoribbons, carried out with approximately 10 W/mL horn sonication, is illustrated by TEM (scale bars, 100 nm). **d**, The threshold length L_{lim} below which a fibril will not break under sonication is determined from plotting sonicated fragment lengths against cross-sectional size, *C*. The yellow areas illustrate the broadened boundaries of the terminal range defined by [$L_{lim}/2$, L_{lim}], and the dashed line represents the average L_{lim}.[48] The tensile strength of AA nanoribbons is calculated to be σ* = 1.87 ± 1.00 GPa. **e**, AA nanoribbon mechanical properties, shown on an Ashby plot, place it among the strongest and stiffest biological materials.[48] Young's modulus and tensile strength values are reported as mean ± standard deviation.

The ultimate tensile strength of AA nanoribbons was determined by AFM statistical analysis after horn sonication-induced scission, which produces nanostructure fragments in water below a threshold length, L_{lim} [44,46]. For clarity, horn sonication delivers 100 to 1000 times greater sonication power intensity to the sample volume compared to bath sonication[47], which was previously shown to reinforce the nanoribbon hydrogen bonding network by ATR-FTIR. From visualizing 400 horn sonicated fragments by TEM (Figure 3c), L_{lim} for the nanoribbons was evaluated from their fragment length distribution as 98 ± 26 nm, which corresponds to a tensile strength of σ* = 1.87 ± 1.00 GPa (Figure 3d, Supplementary Section S3h). These mechanical properties place AA nanoribbons in a region of the Ashby plot viable for solid-state applications (Figure 3e).[48]

Materials constructed of small molecule amphiphile nanoribbons offer high surface areas, on the order of hundreds of m^2/g, dictated by the size of the constituent molecules. The tunable surface chemistries of such structures further allow for targeted interactions, and the capacity for co-assembly of different amphiphiles could allow such materials to perform multiple functions on the same surface[49,50]. However, small molecule nanostructures are often limited to solvated environments due to their fast dynamics and reliance on the hydrophobic effect to hold their structures together. We explored the potential of aligning AA nanoribbons into solid-state thread-like materials, a possibility enabled by their suppressed exchange dynamics and robust mechanical properties.

Alignment of nanoribbons into solid-state threads

A simple strategy for aligning self-assembled nanofibres into 1-dimensional gels in water has been previously demonstrated.[3] In this approach, peptide amphiphiles were thermally annealed to form liquid crystalline bundles, which were shear aligned in divalent counterion solution to produce macroscopic 1-dimensional gels[3]. These gels have been used for applications including cell scaffolding and protein delivery[3,51]. We harnessed this processing strategy by annealing cationic nanoribbons (compound **3**) in water and pulling the suspension through a salt solution (Na_2SO_4) on a glass slide (Figure 1d). This process leads to the formation of a 1-dimensional gel that exhibits birefringence under polarized light (Figure 4a), indicating that the nanoribbons are aligned within the gel. We demonstrate the unique ability of the nanoribbon gel to withstand drying in air, forming a stable solid thread that can be handled, bent without breaking (Figure 1e), and can support over 200 times its weight (Figure 4b). Scanning electron microscopy (SEM) imaging of the AA threads in vacuum reveal thread diameters near 20 μm and striations consistent with the presence of nanoribbon bundles (Supplementary Fig. 29).

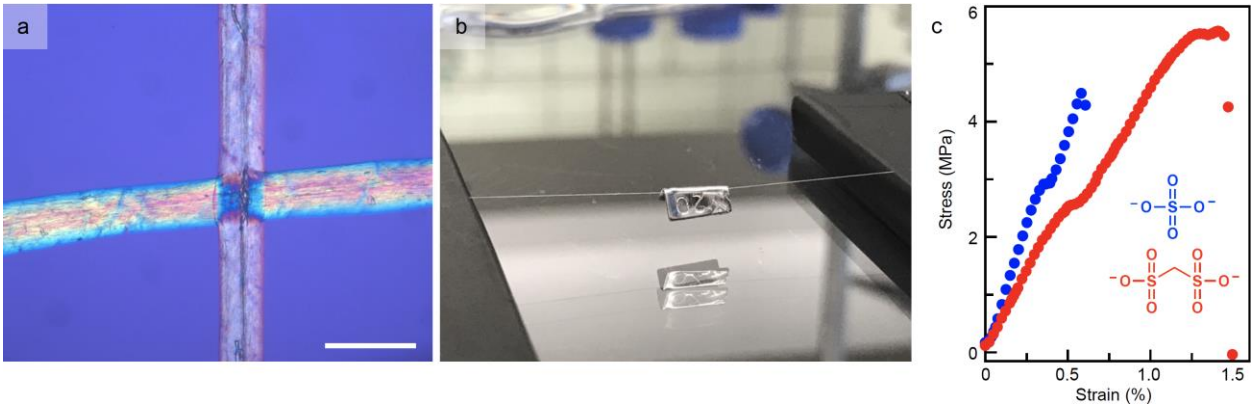

Figure 4. Aramid amphiphile nanoribbons are aligned by shear forces and dried to form flexible threads. a, A polarized light micrograph shows the intersection of two nanoribbon threads. The birefringence observed under cross-polarizers indicates the nanoribbons are aligned within the threads (scale bar, 100 μm). **b**, A 5 cm nanoribbon thread whose mass totals 0.1 mg is suspended over a trough and supports a 20 mg weight. **c**, Representative tensile tests of AA threads formed with sulfate (blue) and methanedisulfonate (red) counterions are shown. Tensile tests of twelve samples reveal Young's moduli of 637 ± 114 MPa and 385 ± 77 MPa, respectively, and extensibility values of 0.6 ± 0.2 % and 1.1 ± 0.2 %, respectively. Data are reported as mean ± standard deviation.

The formation of solid-state nanoribbon threads requires that individual nanoribbons exhibit significant structural integrity, which in the case of AAs is imparted by their aramid domain. However, neither the Young's modulus nor tensile strength of nanoribbons is expected to govern the threads' bulk mechanical properties. Rather, electrostatics dominate interribbon interactions, an effect that has been previously demonstrated at highly charged nanoscale surfaces[52]. We hypothesize that adjusting the nanoribbon surface chemistry and counterion pair provides a route to adjusting the elastic modulus and extensibility of the thread. Consistent with this hypothesis, we find that gelation is only possible when the counterion valency is greater than one.

We performed tensile tests to determine the effect of counterion charge density on the threads' elastic moduli and extensibilities (Figure 4c), providing a benchmark for future studies. Threads formed with two divalent anions, one with a high charge density, sulfate, and one with a lower charge density, methanedisulfonate, were measured. Threads with sulfate and methanedisulfonate counterions produced Young's moduli of 637 ± 114 MPa and 385 ± 77 MPa, respectively (Supplementary Fig. 35). As one point of comparison, the observed modulus values fall on the same order of magnitude as polyethylenes [53]. Further, we find that threads with the methanedisulfonate anion (elongation at break, ε_{break} = 1.1 ± 0.2 %) are nearly twice as extensible as threads formed with the sulfate anion (ε_{break} = 0.6 ± 0.2 %, Supplementary Fig. 36). We attribute the enhanced elastic modulus and decrease in extensibility of threads with sulfate counterions, compared to those with methanedisulfonate counterions, to the enhanced electrostatic interaction strengths between nanoribbons with counterions of greater charge densities[54]. These experiments reveal that nanoribbon surface and counterion chemistry are viable parameters to vary for controlling bulk mechanical properties.

Hierarchical order within dry nanoribbon threads

We used X-ray scattering to study the structure within the nanoribbon thread and to confirm that nanoribbons remain intact after alignment and drying (Figure 5a). Wide-angle X-ray scattering (WAXS) of the dried thread in vacuum shows anisotropic peaks indicating nanoribbon alignment, with the

strongest WAXS peak occurring at a d-spacing of 5.05 Å (Figure 5b). WAXS patterns of vertically oriented nanoribboon threads were collected and integrated to yield meridional and equitorial peaks. From these peaks, a simulated unit cell shows molecular packing resembling poly(*p*-benzamide) (Figure 5c, Supplementary Section S3c) [55]. This structure implies that even upon drying in vacuum, where the hydrophobic effect is absent, intermolecular aramid hydrogen bonding is dominant along the nanoribbon long axis with H-O hydrogen bond distances of 2.08 Å. Further, we infer that π-π stacking at an interplane distance of 3.61 Å laterally holds together hydrogen bonded sheets across the nanoribbon width (Figure 5d).

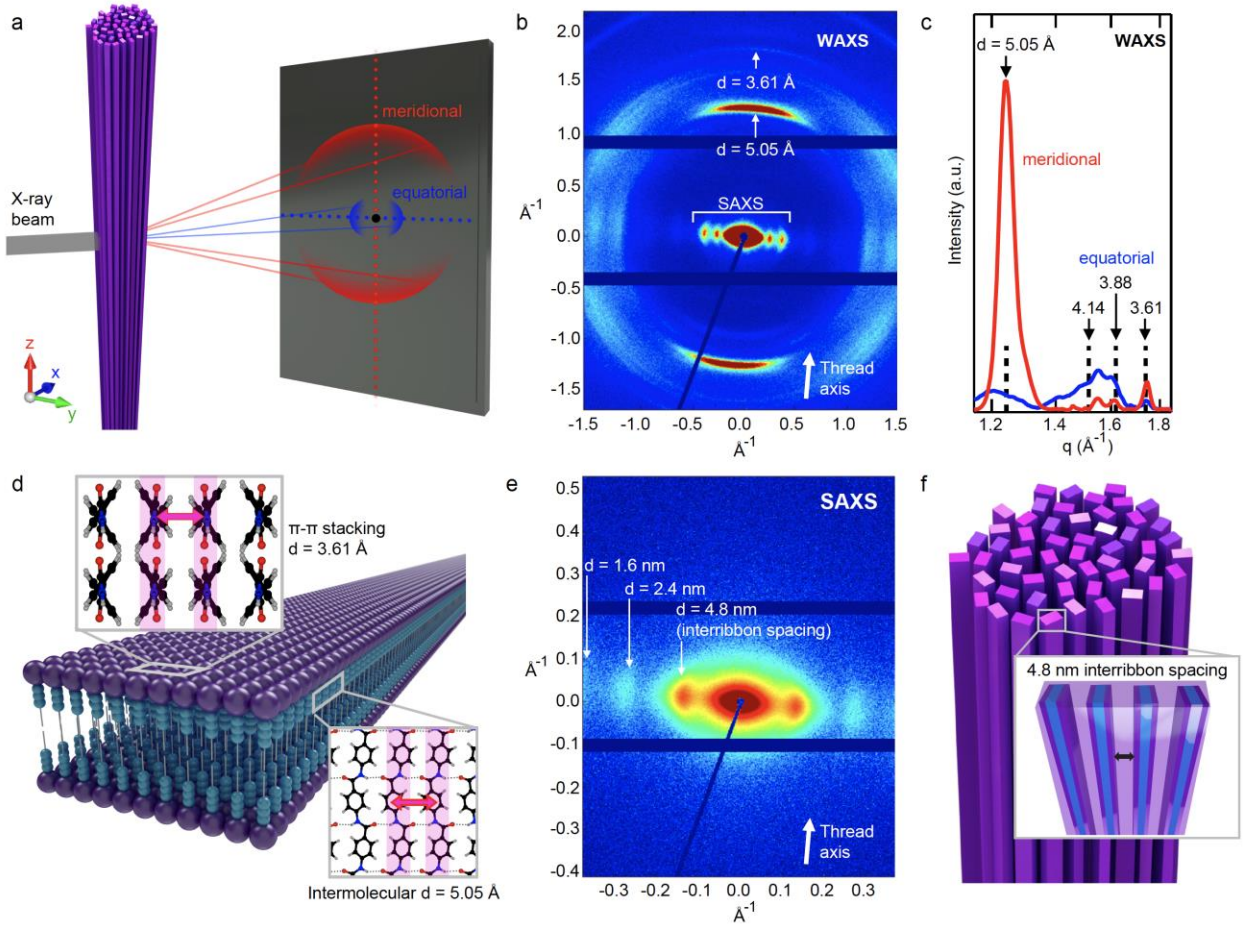

Figure 5. X-ray scattering of solid-state nanoribbon threads demonstrates organized molecular packing, extended hydrogen bonding networks, and long-range hierarchical order. a, Meridional and equatorial scattering directions are depicted in X-ray scattering measurements of solid, aligned AA nanoribbon threads. **b**, A WAXS pattern of an AA nanoribbon thread indicates that precise molecular organization is maintained in the solid state, with significant anisotropy indicating nanoribbon alignment. **c**, A 1-D scattering profile is obtained by integrating meridional and equatorial axes of (b). Black dotted

lines are simulated peak positions of a unit cell with a = 7.22 Å, b = 5.05 Å, and c = 11.10 Å, and space group 26: *P*mc2$_1$ based on poly(*p*-benzamide). **d**, Molecular packing in AA nanoribbons is illustrated as informed by the simulated unit cell in (c). 5.05 Å intermolecular distances are observed, corresponding to H-bonds of 2.08 Å (dotted lines in bottom inset) that form a network down the long-axis of the nanoribbon. 3.61 Å intermolecular π-π stacking lies at a 64º tilt with respect to the hydrogen bonding plane. Based on these distances, the surface area of AA nanoribbons within the thread is 200 m^2/g. **e**, SAXS of an AA nanoribbon thread shows anisotropic lamellar peaks corresponding to a 4.8 nm interribbon spacing. **f**, A hypothesized structure shows the alignment of individual AA nanoribbons to form semi-crystalline domains with 4.8 nm lamellar spacings informed by (e).

The anisotropy observed by X-ray scattering confirms the geometric configuration of the AA structures as nanoribbons within the solid-state thread. The uniform intermolecular distances of 5.05 Å observed along the length of the nanoribbon indicate that an extended hydrogen bonding network is likely unincumbered by torsion or strain. This observation is consistent with the absence of helical nanoribbons, as well as the extraordinary nanoribbon lengths. The attractive forces along the nanoribbon width are significantly weaker, dominated by π-π stacking at an off-ribbon axis angle of 64°. This π-π stacking enables lateral growth of the ribbons, but leads to dimensions of only approximately 5 nm in width. Differences in intermolecular interaction strength along the nanoribbon long axes versus across the widths have previously been shown to lead to high-aspect-ratio nanoribbons as opposed to lamellar sheets.[56]

While X-ray scattering supports the presence of nanoribbon geometries with rectangular cross-sections, this technique is largely insensitive to disordered and highly hydrated domains such as the head group domains of AA nanoribbons. Therefore, the scattering information used to designate the nanoribbons as planar with rectangular cross-sections arises primarily from the structured aramid domains. In reality, the head group domains of the nanoribbon are likely to survey the space surrounding the energetically disfavorable hydrophobic edge, shielding this region from solvent. The ability of the head groups to shield the nanoribbon edge is determined by head group size, hydration, and intermolecular electrostatic repulsion. Consequences of this effect include that the nanoribbon cross-sections are not perfectly rectangular but are rather distorted around the hydrophobic edge. Further, the nanoribbon width should be variable and sensitive to head group chemistry, while the length and thickness are not. To test this hypothesis, we synthesized AAs with neutral oligoethylene glycol head groups (OEG-AA, Supplementary Section S1f). OEG-AA is expected to exhibit minimal head group

repulsion, leading to wider nanoribbons. Upon self-assembly in water, OEG-AA nanoribbon thicknesses and lengths are found to be comparable to nanoribbons of **1**, **2**, and **3**. Consistent with our hypothesis, we find their widths to be greater than those of **1**, **2**, and **3** nanoribbons, measured by cryo-TEM to be 7.0 nm (Supplementary Fig. 24).

Using the dimensions and spacings of compound **3** nanoribbons determined by X-ray scattering, we calculate a surface area within the dried thread as 200 m^2/g. At longer length scales, SAXS peaks in the equatorial direction result from AA nanoribbons aligned along the thread axis (Figure 5e), with 4.8 nm spacings between nanoribbons (Figure 5f). This spacing implies that most of the nanoribbon surfaces are accessible, even in the solid-state. AA threads offer precise internal molecular structure, uniform interribbon spacings, and tunable nanoribbon surface chemistries in a macroscopic 1-dimensional material from small molecule amphiphilic self-assembly [16,17,57].

Conclusions

We have presented a molecular self-assembly platform, the aramid amphiphile (AA). Six hydrogen bonds fix each AA molecule within an extended network, which, when combined with lateral π-π stacking, gives rise to nanoribbons with 4 nm thicknesses, 5-6 nm widths, and lengths of up to 20 μm. These nanoribbons exhibit slow molecular exchange dynamics, and tensile strengths and Young's moduli on the order of gigapascals. We apply a shear alignment technique to form macroscopic threads composed of aligned nanoribbon bundles with uniform 4.8 nm interribbon spacings and surface areas of 200 m^2/g. We propose choice of nanoribbon head group and counterion chemistry as features that may be modified to optimize bulk mechanical properties. Further, we demonstrate that these nanoribbon threads are flexible, can be handled, and can support 200 times their weight, making them suitable for solid-state applications. The aramid amphiphile platform overcomes dynamic instabilities common in supramolecular small molecule assemblies and provides a route to nanostructured, solid-state molecular materials.

References

1 Whitesides, G. M., Mathias, J. P. & Seto, C. T. Molecular self-assembly and nanochemistry: a chemical strategy for the synthesis of nanostructures. *Science* **254**, 1312-1319 (1991).

2 Aida, T., Meijer, E. & Stupp, S. I. Functional supramolecular polymers. *Science* **335**, 813-817 (2012).

3 Zhang, S. *et al.* A self-assembly pathway to aligned monodomain gels. *Nat. Mater.* **9**, 594-601 (2010).

4 Koutsopoulos, S., Unsworth, L. D., Nagai, Y. & Zhang, S. Controlled release of functional proteins through designer self-assembling peptide nanofiber hydrogel scaffold. *Proc. Natl. Acad. Sci. USA* **106**, 4623-4628 (2009).

5 Tantakitti, F. *et al.* Energy landscapes and functions of supramolecular systems. *Nat. Mater.* **15**, 469 (2016).

6 Ortony, J. H. *et al.* Internal dynamics of a supramolecular nanofibre. *Nat. Mater.* **13**, 812 (2014).

7 Schief, W., Touryan, L., Hall, S. & Vogel, V. Nanoscale topographic instabilities of a phospholipid monolayer. *J. Phys. Chem. B* **104**, 7388-7393 (2000).

8 Da Silva, R. M. *et al.* Super-resolution microscopy reveals structural diversity in molecular exchange among peptide amphiphile nanofibres. *Nat. Commun.* **7**, 11561 (2016).

9 Wimley, W. C. & Thompson, T. E. Transbilayer and interbilayer phospholipid exchange in dimyristoylphosphatidylcholine/dimyristoylphosphatidylethanolamine large unilamellar vesicles. *Biochemistry* **30**, 1702-1709 (1991).

10 Ortony, J. H. *et al.* Water Dynamics from the Surface to the Interior of a Supramolecular Nanostructure. *J. Am. Chem. Soc.* **139**, 8915-8921 (2017).

11 Yuan, D., Shi, J., Du, X., Zhou, N. & Xu, B. Supramolecular glycosylation accelerates proteolytic degradation of peptide nanofibrils. *J. Am. Chem. Soc.* **137**, 10092-10095 (2015).

12 Toledano, S., Williams, R. J., Jayawarna, V. & Ulijn, R. V. Enzyme-triggered self-assembly of peptide hydrogels via reversed hydrolysis. *J. Am. Chem. Soc.* **128**, 1070-1071 (2006).

13 Freeman, R. *et al.* Reversible self-assembly of superstructured networks. *Science* **362**, 808-813 (2018).

14 Williams, R. J. *et al.* Enzyme-assisted self-assembly under thermodynamic control. *Nat. Nanotechnol.* **4**, 19 (2009).

15 Hashim, P., Bergueiro, J., Meijer, E. & Aida, T. Supramolecular Polymerization: A Conceptual Expansion for Innovative Materials. *Prog. Polym. Sci.* **105**, 101250 (2020).

16 Xu, Y. *et al.* Nanostructured polymer films with metal-like thermal conductivity. *Nat. Commun.* **10**, 1-8 (2019).

17 Tuller, H. L. Ionic conduction in nanocrystalline materials. *Solid State Ionics* **131**, 143-157 (2000).

18 Sherrington, D. C. & Taskinen, K. A. Self-assembly in synthetic macromolecular systems via multiple hydrogen bonding interactions. *Chem. Soc. Rev.* **30**, 83-93 (2001).

19 Dobb, M., Johnson, D. & Saville, B. Supramolecular structure of a high‐modulus polyaromatic fiber (Kevlar 49). *J. Polymer Sci. Polymer Phys. Ed.* **15**, 2201-2211 (1977).

20 Seyler, H., Storz, C., Abbel, R. & Kilbinger, A. F. A facile synthesis of aramide–peptide amphiphiles. *Soft Matter* **5**, 2543-2545 (2009).

21 Claussen, R. C., Rabatic, B. M. & Stupp, S. I. Aqueous self-assembly of unsymmetric peptide bolaamphiphiles into nanofibers with hydrophilic cores and surfaces. *J. Am. Chem. Soc.* **125**, 12680-12681 (2003).

22 Yang, M. *et al.* Dispersions of aramid nanofibers: a new nanoscale building block. *ACS nano* **5**, 6945-6954 (2011).

23 Schleuss, T. W. *et al.* Hockey-Puck Micelles from Oligo(p-benzamide)-b-PEG Rod–Coil Block Copolymers. *Angew. Chem. Int. Ed.* **45**, 2969-2975, doi:10.1002/anie.200503514 (2006).

24 Bohle, A. *et al.* Hydrogen-Bonded Aggregates of Oligoaramide−Poly(ethylene glycol) Block Copolymers. *Macromolecules* **43**, 4978-4985, doi:10.1021/ma100501j (2010).
25 Abbel, R., Schleuss, T. W., Frey, H. & Kilbinger, A. F. M. Rod-Length Dependent Aggregation in a Series of Oligo(p-benzamide)-Block-Poly(ethylene glycol) Rod-Coil Copolymers. *Macromol. Chem. Phys.* **206**, 2067-2074, doi:10.1002/macp.200500259 (2005).
26 Johansson, A., Kollman, P., Rothenberg, S. & McKelvey, J. Hydrogen bonding ability of the amide group. *J. Am. Chem. Soc.* **96**, 3794-3800 (1974).
27 Dixon, D. A., Dobbs, K. D. & Valentini, J. J. Amide-water and amide-amide hydrogen bond strengths. *J. Phys. Chem.* **98**, 13435-13439 (1994).
28 Kline, S. R. Reduction and analysis of SANS and USANS data using IGOR Pro. *J. Appl. Crystallogr.* **39**, 895-900 (2006).
29 Nallet, F., Laversanne, R. & Roux, D. Modelling X-ray or neutron scattering spectra of lyotropic lamellar phases: interplay between form and structure factors. *J. Phys. II* **3**, 487-502 (1993).
30 Mertens, H. D. & Svergun, D. I. Structural characterization of proteins and complexes using small-angle X-ray solution scattering. *J. Struct. Biol.* **172**, 128-141 (2010).
31 Yokoi, H., Kinoshita, T. & Zhang, S. Dynamic reassembly of peptide RADA16 nanofiber scaffold. *Proc. Natl. Acad. Sci. USA* **102**, 8414-8419 (2005).
32 Hartgerink, J. D., Beniash, E. & Stupp, S. I. Self-assembly and mineralization of peptide-amphiphile nanofibers. *Science* **294**, 1684-1688 (2001).
33 Cravotto, G. & Cintas, P. Molecular self-assembly and patterning induced by sound waves. The case of gelation. *Chem. Soc. Rev.* **38**, 2684-2697 (2009).
34 Gorelik, T. E., van de Streek, J., Kilbinger, A. F., Brunklaus, G. & Kolb, U. Ab-initio crystal structure analysis and refinement approaches of oligo p-benzamides based on electron diffraction data. *Acta Crystallogr. Sect. B: Struct. Sci.* **68**, 171-181 (2012).
35 Gorelik, T. *et al.* H-bonding schemes of di-and tri-p-benzamides assessed by a combination of electron diffraction, X-ray powder diffraction and solid-state NMR. *CrystEngComm* **12**, 1824-1832 (2010).
36 Wang, J., Liu, K., Xing, R. & Yan, X. Peptide self-assembly: thermodynamics and kinetics. *Chem. Soc. Rev.* **45**, 5589-5604 (2016).
37 Barth, A. Infrared spectroscopy of proteins. *Biochim. Biophys. Acta, Bioenerg.* **1767**, 1073-1101 (2007).
38 Zandomeneghi, G., Krebs, M. R., McCammon, M. G. & Fändrich, M. FTIR reveals structural differences between native β‐sheet proteins and amyloid fibrils. *Protein Sci.* **13**, 3314-3321 (2004).
39 Matayoshi, E. D., Wang, G. T., Krafft, G. A. & Erickson, J. Novel fluorogenic substrates for assaying retroviral proteases by resonance energy transfer. *Science* **247**, 954-958 (1990).
40 Wu, B., Heidelberg, A. & Boland, J. J. Mechanical properties of ultrahigh-strength gold nanowires. *Nat. Mater.* **4**, 525-529 (2005).
41 Smith, J. F., Knowles, T. P., Dobson, C. M., MacPhee, C. E. & Welland, M. E. Characterization of the nanoscale properties of individual amyloid fibrils. *Proc. Natl. Acad. Sci. USA* **103**, 15806-15811 (2006).
42 Knowles, T. P. *et al.* Role of intermolecular forces in defining material properties of protein nanofibrils. *Science* **318**, 1900-1903 (2007).
43 Lamour, G., Kirkegaard, J. B., Li, H., Knowles, T. P. & Gsponer, J. Easyworm: an open-source software tool to determine the mechanical properties of worm-like chains. *Source Code Biol. Med.* **9**, 16 (2014).
44 Huang, Y. Y., Knowles, T. P. & Terentjev, E. M. Strength of nanotubes, filaments, and nanowires from sonication‐induced scission. *Adv. Mater.* **21**, 3945-3948 (2009).
45 Nassar, R., Wong, E., Gsponer, J. & Lamour, G. Inverse Correlation between Amyloid Stiffness and Size. *J. Am. Chem. Soc.* **141**, 58-61, doi:10.1021/jacs.8b10142 (2019).

46 Peng, Z. *et al.* High Tensile Strength of Engineered β-Solenoid Fibrils via Sonication and Pulling. *Biophys. J.* **113**, 1945-1955, doi:10.1016/j.bpj.2017.09.003 (2017).
47 Santos, H. M., Lodeiro, C. & Capelo-Martínez, J.-L. in *Ultrasound in chemistry: analytical applications* 1-16 (Wiley Online Library, 2009).
48 Lamour, G. *et al.* Mapping the broad structural and mechanical properties of amyloid fibrils. *Biophys. J.* **112**, 584-594 (2017).
49 Zhao, X. *et al.* Molecular self-assembly and applications of designer peptide amphiphiles. *Chem. Soc. Rev.* **39**, 3480-3498 (2010).
50 Niece, K. L., Hartgerink, J. D., Donners, J. J. & Stupp, S. I. Self-assembly combining two bioactive peptide-amphiphile molecules into nanofibers by electrostatic attraction. *J. Am. Chem. Soc.* **125**, 7146-7147 (2003).
51 Angeloni, N. L. *et al.* Regeneration of the cavernous nerve by Sonic hedgehog using aligned peptide amphiphile nanofibers. *Biomaterials* **32**, 1091-1101 (2011).
52 Fink, L., Steiner, A., Szekely, O., Szekely, P. & Raviv, U. Structure and interactions between charged lipid membranes in the presence of multivalent ions. *Langmuir* **35**, 9694-9703 (2019).
53 Knowles, T. P. & Buehler, M. J. Nanomechanics of functional and pathological amyloid materials. *Nat. Nanotechnol.* **6**, 469-479 (2011).
54 Bradbury, R. & Nagao, M. Effect of charge on the mechanical properties of surfactant bilayers. *Soft Matter* **12**, 9383-9390 (2016).
55 Takahashi, Y., Ozaki, Y., Takase, M. & Krigbaum, W. Crystal structure of poly (p‐benzamide). *J. Polym. Sci., Part B: Polym. Phys.* **31**, 1135-1143 (1993).
56 Paramonov, S. E., Jun, H.-W. & Hartgerink, J. D. Self-assembly of peptide− amphiphile nanofibers: the roles of hydrogen bonding and amphiphilic packing. *J. Am. Chem. Soc.* **128**, 7291-7298 (2006).
57 Russell, P. Photonic crystal fibers. *Science* **299**, 358-362 (2003).

Acknowledgements

We thank Elad Deiss-Yehiely and Charlie Settens for their helpful input. We thank Ryan Allen and Lee Hopkins for contributing graphics shown in the figures. We acknowledge Jia Tian and Shantanu Kallakuri for contributions to synthesis of early stage aramid amphiphiles that led to the molecular designs incorporated in this report. **Funding:** This material is based upon work supported by the National Science Foundation under Grant No. CHE-194550. This work was supported in part by the Professor Amar G. Bose Research Grant Program, the Abdul Latif Jameel Water and Food Systems Lab, and the MIT Center for Environmental Health Sciences under NIH Center grant P30-ES002109. D.-Y.K. acknowledges the support of the National Research Foundation of Korea's Basic Science Research Program and Chonbuk National University Fellowship Program. T.C.-T. and W.R.L. acknowledge the support of the National Science Foundation Graduate Research Fellowship Program under Grant No. 1122374. T.C.-T. acknowledges the support of the Martin Family Society of Fellows for Sustainability.

G.L. acknowledges support from the Université d'Evry-Paris Saclay. This work made use of the U.S. Army's Institute for Soldier Nanotechnologies at MIT; the MRSEC Shared Experimental Facilities at MIT supported by the National Science Foundation under award number DMR-14-19807; and the MIT Department of Chemistry Instrumentation Facility (DCIF). X-ray scattering measurements were performed at beamline 12-ID-B of the Advanced Photon Source, a U.S. Department of Energy (DOE) Office of Science User Facility operated for the DOE Office of Science by Argonne National Laboratory under Contract No. DE-AC02-06CH11357; This work was performed in part at the Harvard University Center for Nanoscale Systems (CNS) cryo-TEM facility, a member of the National Nanotechnology Coordinated Infrastructure Network (NNCI), which is supported by the National Science Foundation under NSF award no. 1541959.

Author Contributions

T.C.-T., D.-Y. K., and J.H.O. conceived and designed the experiments. D.-Y.K. and T.C.-T. synthesized materials with assistance from W.R.L. and A.J.L.. T.C.-T. and D.-Y.K. performed chemical characterization of all samples. T.C.-T. performed conventional TEM and cryo-TEM. Y.C. and T.C.-T. performed SEM. G.L. performed AFM and statistical topographical analyses. G.L. performed sonication-induced scission measurements, imaging with AFM and TEM, and analysis of data. A.J.L. performed FRET measurements and analysis of the data. X.Z., T.C.-T., and Y.C. performed solution X-ray scattering, and analysis of the data. A.J.L. and Y.C. conceptualized nanoribbon thread processing and Y.C. and M.G. prepared nanoribbon threads. M.G. performed tensile testing of nanoribbon threads and analysis of the data. T.C.-T. and Y.C. performed X-ray scattering of solid-state nanoribbon threads and analysis of the data. J.H.O., T.C.-T, and Y.C. co-wrote the manuscript. J.H.O. provided project administration, funding acquisition, and supervision. All authors discussed the results and commented on the manuscript.

Data availability

The data generated and analyzed during this study are available from the corresponding author on reasonable request.

Additional Information

Supplementary information is available in the online version of the paper. Reprints and permission information is available online at www.nature.com/reprints. Correspondence and requests for materials should be addressed to J.H.O.

Competing Interests

The authors declare no competing interests.

Figure Captions

Figure 2. Kevlar-inspired aramid amphiphiles self-assemble into ultra-stable nanoribbons capable of hierarchical ordering to form dry macroscopic threads. a, Aramid amphiphiles are composed of a charged head group and an aliphatic tail to induce amphiphilic self-assembly, and an aramid structural domain to yield collective intermolecular hydrogen bonding. Aramid amphiphiles **1**, **2**, and **3** have anionic, zwitterionic, and cationic head groups, respectively. **b**, Aramid amphiphiles are designed to spontaneously self-assemble in water into nanoribbons with suppressed exchange dynamics. **c**, Dried nanoribbons of **2** are observed in a representative transmission electron micrograph (TEM) (scale bar, 1 μm). **d**, A nanoribbon suspension (compound **3**) is pulled out of a pipet tip by tweezers into a sodium sulfate solution to form a 1-dimensional gel. **e,** The gel is removed from water and dried to form a thread composed of aligned nanoribbons that can be bent and handled easily.

Figure 2. Aramid amphiphile nanoribbons exhibit minimal molecular exchange. a, Small angle X-ray scattering of **1**, **2**, and **3** nanoribbons in water shows a slope of -2 in the low-*q* regime, indicating high-aspect-ratio structures, and is best fit to a lamellar model (black line) giving a 3.9 nm nanoribbon thickness, consistent with nanoribbon geometries. **b**, Representative cryogenic TEM of nanoribbons of **2** in water reveals nanoribbon widths of approx. 5 nm (scale bar, 100 nm). **c**, ATR-FTIR of compound **3** nanoribbons shows the emergence of a sharp peak at 1638 cm^{-1} upon bath sonication, consistent with strengthening of the hydrogen bond network. **d**, Normalized fluorescence intensities of a 1:1 mixture of donor- and quencher-labeled nanoribbon suspensions are measured over 55 days. A nearly constant fluorescence intensity indicates minimal dark quenching and corresponds to minimal molecular exchange between nanoribbons over this time period. As a control, complete co-assembly of donor and quencher amphiphiles result in a 76% decrease in fluorescence intensity, illustrated by the horizontal dotted line (Supplementary Section S3f). **e**, Normalized fluorescence intensities of mixtures of donor- and quencher-labeled nanoribbon suspensions at 80 °C show that FRET dark quenching is not observed upon heating. This experiment was carried out with AA concentrations ranging from 0.1 to 0.5 mM, and no changes in exchange were observed.

Figure 3. Aramid amphiphile nanoribbons have a Young's modulus of E = 1.7 GPa, and a tensile strength of σ* = 1.9 GPa. a, Contours acquired by tracing the AFM profiles of 29 AA nanoribbons are used for statistical topographical analysis (scale bar, 1 μm). **b**, Midpoint deviations δ from contour traces are used to calculate a persistence length, P = 3.9 ± 0.7 μm and Young's modulus, E = 1.7 ± 0.7 GPa, from least-squares fitting of a worm-like chain model for semi-flexible polymers to the data. **c**, Sonication-induced scission of nanoribbons, carried out with approximately 10 W/mL horn sonication, is illustrated by TEM (scale bars, 100 nm). **d**, The threshold length L_{lim} below which a fibril will not break under sonication is determined from plotting sonicated fragment lengths against cross-sectional size, *C*. The yellow areas illustrate the broadened boundaries of the terminal range defined by [L_{lim}/2, L_{lim}], and the dashed line represents the average L_{lim}.[48] The tensile strength of AA nanoribbons is calculated to be σ* = 1.87 ± 1.00 GPa. **e**, AA nanoribbon mechanical properties, shown on an Ashby plot, place it among the strongest and stiffest biological materials.[48] Young's modulus and tensile strength values are reported as mean ± standard deviation.

Figure 4. Aramid amphiphile nanoribbons are aligned by shear forces and dried to form flexible threads. a, A polarized light micrograph shows the intersection of two nanoribbon threads. The birefringence observed under cross-polarizers indicates the nanoribbons are aligned within the threads (scale bar, 100 μm). **b**, A 5 cm nanoribbon thread whose mass totals 0.1 mg is suspended over a trough and supports a 20 mg weight. **c**, Representative tensile tests of AA threads formed with sulfate (blue) and methanedisulfonate (red) counterions are shown. Tensile tests of twelve samples reveal Young's moduli of 637 ± 114 MPa and 385 ± 77 MPa, respectively, and extensibility values of 0.6 ± 0.2 % and 1.1 ± 0.2 %, respectively. Data are reported as mean ± standard deviation.

Figure 5. X-ray scattering of solid-state nanoribbon threads demonstrates organized molecular packing, extended hydrogen bonding networks, and long-range hierarchical order. a, Meridional and equatorial scattering directions are depicted in X-ray scattering measurements of solid, aligned AA nanoribbon threads. **b**, A WAXS pattern of an AA nanoribbon thread indicates that precise molecular organization is maintained in the solid state, with significant anisotropy indicating nanoribbon alignment. **c**, A 1-D scattering profile is obtained by integrating meridional and equatorial axes of (b). Black dotted lines are simulated peak positions of a unit cell with a = 7.22 Å, b = 5.05 Å, and c = 11.10 Å, and space group 26:*P*mc2$_1$ based on poly(*p*-benzamide). **d**, Molecular packing in AA nanoribbons is illustrated as informed by the simulated unit cell in (c). 5.05 Å intermolecular distances are observed, corresponding to H-bonds of 2.08 Å (dotted lines in bottom inset) that form a network down the long-axis of the nanoribbon. 3.61 Å intermolecular π-π stacking lies at a 64° tilt with respect to the hydrogen bonding plane. Based on these distances, the surface area of AA nanoribbons within the thread is 200 m^2/g. **e**, SAXS of an AA nanoribbon thread shows anisotropic lamellar peaks corresponding to a 4.8 nm interribbon spacing. **f**, A hypothesized structure shows the alignment of individual AA nanoribbons to form semi-crystalline domains with 4.8 nm lamellar spacings informed by (e).

Methods

Synthesis of aramid amphiphiles (AAs)

The syntheses used in this study involve: 1) carbodiimide-mediated coupling reactions to form amide linkages, 2) conventional deprotection reactions of *tert*-butyloxycarbonyl (Boc), and 3) hydrolysis of ester functionalities to produce carboxylic acid moieties. As the only exception, the zwitterionic head group of **2** is obtained by quaternization of a tertiary amine with a propanesultone. ^{1}H and ^{13}C nuclear magnetic resonance (NMR, Supplementary Section S2a, Bruker Avance III DPX 400) and mass spectrometry (MS, Supplementary Section S2b, Bruker Omniflex) were used to confirm the chemical composition of intermediates and products. The observed solubilities of **1** and **2** are up to 1.0 mg/mL, and the solubility of **3** exceeds 20 mg/mL. Synthesis details on each of compounds **1**, **2**, **3**, **OEG-AA**, and the FRET donor- and quencher-labeled AAs and their intermediates are provided in Supplementary Section 1.

Shear alignment to form macroscopic aramid amphiphile (AA) threads

A 2.0 wt% aqueous solution of **3** was bath sonicated for 24 h, rested for 12 h, annealed in a heating block at 80 °C for 10 h, and then slowly cooled to room temperature. This solution was extruded into a bath of 40. mM sodium sulfate (Na_2SO_4) or 40. mM disodium methanedisulfonate ($Na_2CH_2S_2O_6$) to produce 1-dimensional gels, which are pulled out of the solution and dried under ambient conditions to form the final macroscopic aramid amphiphile threads.

Attenuated total reflectance Fourier-transform infrared spectroscopy

ATR-FTIR spectra of aqueous samples of compound **3** dissolved at a 20 mg/mL concentration in deuterated water (D_2O) were acquired using an attenuated total reflectance-infrared spectroscope (Bruker ALPHA II) at room temperature with a diamond crystal. Three different solvent ratios were used (D_2O:DMSO = 50:50, 75:25 and 100:0), and spectra were captured upon mixing sample into the solvent as well as with 10 min, 1 h, and 24 h of bath sonication after mixing (Supplementary Figs. 19-20). Solvent background with the same sonication time was subtracted from each spectra and the spectra were

normalized to the amide I stretching peak at 1672 cm^{-1}. D_2O was selected in place of water to provide less interference in the IR region of interest.

The spectra of compound **3** and **4** powders (Supplementary Fig. 19) were acquired by transmission IR on a ThermoFisher Scientific Nicolet 6700. Potassium bromide (KBr)-amphiphile pellets were prepared by mixing 0.1 mg of compound **3** powder with 0.5 g of KBr (Fisher Scientific, FTIR grade). The ambient background of carbon dioxide-free air was subtracted from the spectra.

Transmission electron microscopy

Transmission electron microscopy (TEM) images were captured on a FEI Tecnai G2 Spirit TWIN microscope at an accelerating voltage of 120 kV. Grids were prepared by depositing 10. μL of a 1 mg/mL amphiphile solution onto a continuous carbon grid (Electron Microscopy Sciences, 200 mesh, copper) for 20 sec, blotting to remove the solution, depositing 10. μL of a 0.1% phosphotungstic acid solution onto the grid (Electron Microscopy Sciences), and blotting to remove the stain. TEM images of **1**, **2**, and **3** are shown in Supplementary Fig. 21.

X-ray scattering

Solution small angle X-ray scattering (SAXS) samples were prepared by dissolving lyophilized powders of **1**, **2**, and **3** in DI water above the solubility limit. To avoid artifacts associated with nanostructure aggregation, each sample was centrifuged at 3,000 rpm and its supernatant was loaded into 2 mm diameter quartz capillary tubes (Hampton Research). Variable temperature SAXS profiles (Figure S26) were performed on compounds **1** and **2** in water at 1 mg/mL, and **3** at 20 mg/mL.

Solution SAXS measurements (Figures 2a and S26) and WAXS measurements on nanoribbon threads (Figure S27) were performed at Beamline 12-ID-B of Advanced Photon Source at Argonne National Laboratory with an X-ray radiation energy of 13.3 keV. DECTRIS PILATUS 300K and PILATUS 2M detectors were used for SAXS and WAXS, respectively. The 2-D X-ray scattering patterns were background subtracted to remove water and capillary background, and processed using beamline

software for reduction to 1-D data curves. The higher resolution of the compound **3** SAXS profile relative to those of compounds **1** and **2** is due the notably higher solubility of compound **3**.

Wide angle X-ray scattering (WAXS) and SAXS measurements on dried macroscopic aramid amphiphile threads presented in Figure 5 were performed in vacuum on a SAXSLAB instrument using a Rigaku 002 microfocus X-ray source (CuK_α radiation, 1.5418Å) and a DECTRIS PILATUS 300K detector. WAXS and SAXS profiles were measured at a sample-to-detector distance of 109 mm and 459 mm, respectively. Descriptions of fitting for all X-ray scattering experiments are described in Supplementary Section S3c.

Cryogenic transmission electron microscopy

Cryogenic transmission electron microscopy (cryo-TEM) grids were prepared with an FEI Vitrobot Mark IV. Holey carbon grids (Ted Pella, 300 mesh, copper) were glow-discharged before a 3.0 μL drop of a 2.0 mg/mL amphiphile solution was pipetted onto the grids in a chamber with 100% humidity. The grids were blotted for 4 sec, and then plunged into C_2H_6 (*l*) followed by N_2 (*l*). Images were captured in an FEI Tecnai Arctica microscope at an accelerating voltage of 200 kV. The defocus in data collection ranged from -1.5 to -3.5 μm.

Observation of nanoribbon length by atomic force microscopy

Compound **3** solution (2.0 wt%) was prepared for AFM by following the sonication and heat treatment for making nanoribbon thread solutions prior to their shear alignment: bath sonication for 24 h, resting for 12 h, annealing in a heating block at 80 °C for 10 h, and then slow cooling to room temperature. The solution was then diluted to 0.01 wt% and a 100. μL droplet of this diluted solution was deposited onto a cleaned mica substrate and analyzed by AFM. The mica substrate was prepared through plane cleavage and cleaning with DI H_2O. After 3 h of incubating the amphiphile solution on the clean mica, the solution was removed and then used directly for AFM imaging. Nanoribbons were imaged in tapping mode in air using a Cypher (Asylum Research, Oxford Instruments) atomic force microscope. We

used AC160TS-R3 cantilevers from Olympus (nominal spring constant 26 N/m and resonance frequency of 300 kHz in air). AFM images were recorded at 512 px × 512 px at a scanning speed of 0.65 Hz.

Scanning electron microscopy

Scanning electron microscopy (SEM) images were recorded on a Zeiss MERLIN field emission microscope operating at a 1-3 kV accelerating voltage to resolve higher-order structure of the dried AA nanoribbon threads. A secondary electron detector set to 120-200 pA was used for imaging. The SEM micrograph in Supplementary Fig. 29 was coated with 10 nm Au by sputtering on a MS Q150T ES coater.

Förster resonance energy transfer

A fluorescent donor (EDANS) and quencher (DABCYL) were each covalently tethered to the head group region of an AA (Supplementary Fig. 31). AAs were prepared at concentrations of 0.1 to 0.5 mM in water and co-assembled with 5 mol% donor- or quencher-tagged analogues. Fluorescence intensities were measured on a Varian Cary Eclipse spectrophotometer operating at an excitation wavelength of 334 nm with excitation and emission slits set at 5 nm. A fluorimeter scan rate of 600 nm/min was used, and the PMT detector voltage was 600 V. A further description of the FRET study and control experiments is provided in Supplementary Section S3f.

Stiffness determination by topographical analysis of nanoribbon contours

Compound **3** nanoribbons were imaged in tapping mode in water using a Bruker/JPK Nanowizard 4 atomic force microscope using BL-AC40-TS cantilevers from Olympus (nominal spring constant 0.1 N/m and resonance frequency of ~25 kHz in water). AFM images were recorded at 512 px × 512 px at a scanning speed of 10 Hz. Fluctuations of ribbon shapes from AFM images were statistically processed using the Easyworm software tool[43], which traces parametric splines to the contours of many ribbons of the same sample (in this experiment, n = 29 ribbons). The persistence length *P* extracted from this data is used to calculate each nanoribbons' flexural rigidity by scaling to thermal energy, and the Young's

modulus *E* is ultimately evaluated by dividing the flexural rigidity by the area moment of inertia for the nanoribbon. A detailed description of sample preparation and experimental details is provided in Supplementary Section S3g.

Yield strength determination by sonication-induced scission

We measure the yield (tensile) strength σ^* by a sonication-induced fibril scission technique, as detailed in our previous work[48]. In short, sonication creates collapsing cavitation bubbles, causing fluid velocity fields to trap fibrils and exert shear forces on them. This leads to fibril extension in opposite directions and mechanically-induced rupture at the site of highest stress. After prolonged sonication time, fibril length distribution reaches a plateau and the size of fragments that belong to a sample fall in a "terminal range" correlated to the yield strength of the nanoribbons.

A Qsonica Q500 sonicator with a 2-mm-diameter microtip was used to sonicate 10 mL of a 0.5 mg/mL aqueous solution of compound 3 nanoribbons. A vibrational frequency of 20 kHz and amplitude of 25% were used during the experiment, which lasted for 2 h of "sonication on" time with a 5 sec on/3 sec off pulse. Sonicating power was held at 30 W/cm^2 to ensure cavitation. The solution was held in an ice bath for the duration of the experiment to prevent solvent evaporation and tip breakage during sonication. Images of fragments after sonication were captured by TEM and AFM. A comprehensive discussion on this experimental technique is provided in Supplementary Section S3h.

Polarized light microscopy

The liquid crystalline state of gelled AA nanoribbons was observed using an Olympus BH-2 microscope equipped for polarized light imaging. Gelled nanoribbons were analyzed immedaitely after extrusion onto a cleaned glass microscope slide while still wet. Images were captured with a Pixelink PL-E535CU camera.

Tensile testing of macroscopic AA threads

Macroscopic mechanical properties of compound **3** AA threads were characterized using a uniaxial bench-top tester (CellScale UStretch) equipped with a 0.5 N load cell. Threads were prepared following the shear alignment procedure described previously, then fixed with epoxy glue on two tailored carboard supports gripped to the standard spring-loaded clamps of the testing machine. The glue was allowed to set for 24 h. Threads with counterions of either sulfate (n=6) or methanedisulfonate (n=6) were tested at a constant stretch velocity of 25 μm/s. Each thread was imaged with an optical microscope to determine its mean diameter from multiple cross-sections, which varied between 55 μm and 80 μm for all threads.

Raw data from the UStretch software was exported and analyzed separetly in MATLAB. Force measurements were converted to stress using the initial cross-sectional area. Displacement of the moving end (u_L) was converted into engineering strain using the initial length of each thread (L_0) as u_L / L_0. The Young's modulus was extracted by fitting each experiment to a linear elastic constitutive equation using a nonlinear least squares algorithm. The extensibility (maximum strain at failure) was extracted directly from the stress-strain curves at the maximum stress before breakage. Values are reported as average ± one standard deviation.

Method References

43 Lamour, G., Kirkegaard, J. B., Li, H., Knowles, T. P. & Gsponer, J. Easyworm: an open-source software tool to determine the mechanical properties of worm-like chains. *Source Code Biol. Med.* **9**, 16 (2014).

48 Lamour, G. *et al.* Mapping the broad structural and mechanical properties of amyloid fibrils. *Biophys. J.* **112**, 584-594 (2017).

Supplementary Information for

Self-assembly of aramid amphiphiles into ultra-stable nanoribbons and aligned nanoribbon threads

Ty Christoff-Tempesta, Yukio Cho, Dae-Yoon Kim, Michela Geri, Guillaume Lamour, Andrew J. Lew, Xiaobing Zuo, William R. Lindemann, Julia H. Ortony*

*Correspondence to: ortony@mit.edu

This PDF file includes:

S1. Synthesis and methods

S1a. Materials

Methyl 4-aminobenzoate (Sigma Aldrich, 98%), 3,3-dimethylbutyric acid (Sigma Aldrich, 98%), *N*,*N*-dimethyl-*p*-phenylenediamine (DPP, Sigma Aldrich, 97%), *N*-Boc-*p*-phenylenediamine (BPP, Sigma Aldrich, 97%), 1,3-propanesultone (PPS, Sigma Aldrich, 99%), 1,4-bis-Boc-1,4,7-triazaheptane (BBT, Chem Impex, 100%), diethylenetriamine-*N*,*N*,*N''*,*N''*-tetra-*tert*-butyl acetate-*N'*-acetic acid (DPTA, Combi Blocks, 95%), methoxypolyethylene glycol amine (Sigma Aldrich), 1-ethyl-3-(3-dimethylaminopropyl)carbodiimide hydrochloride (EDC, TCI Chemicals, 98%), 4-dimethylaminopyridine (DMAP, TCI Chemicals, 99%), 1-hydroxybenzotriazole hydrate (HOBt, TCI Chemicals, 97%), *N*,*N*-Diisopropylethylamine (DIPEA, Alfa Aesar, 99%), lithium hydroxide (LiOH, Alfa Aesar, 98%), sodium bicarbonate ($NaHCO_3$, Alfa Aesar, 99%), hydrochloric acid (HCl, Alfa Aesar, 36%), sodium sulfate (Na_2SO_4, Fisher Scientific, 99%), and trifluoroacetic acid (TFA, Alfa Aesar, 99%) were used as received without further purification.

S1b. Anionic amphiphile and its intermediates

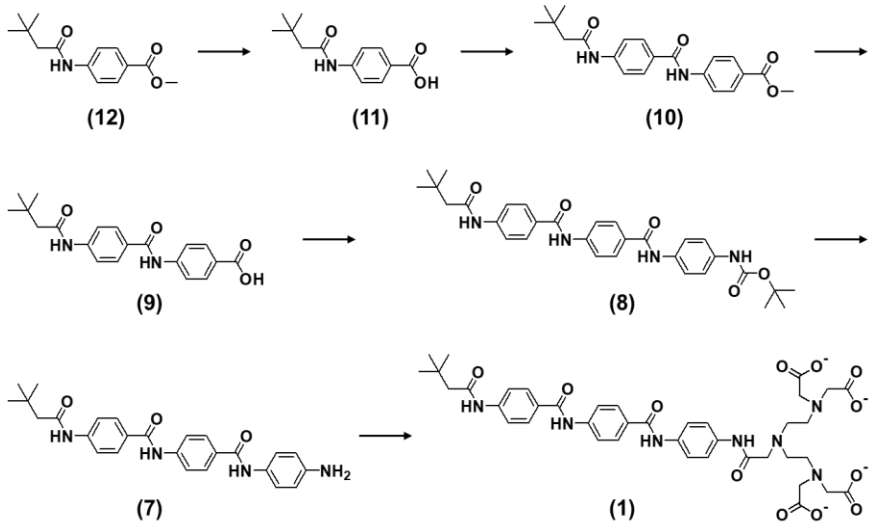

Supplementary Scheme 1. Synthesis scheme to obtain anionic amphiphile.

Methyl 4-(3,3-dimethylbutanamido)benzoate (**12**): A solution of methyl 4-aminobenzoate (11.01 mmol), 3,3-dimethylbutyric acid (16.52 mmol), EDC (33.03 mmol), and DMAP (33.03 mmol) in tetrahydrofuran (50 mL) was stirred at room temperature for 24 h. After the reaction, the solvent was removed in vacuum, and the residue was washed with distilled water and extracted in chloroform. The organic layer was purified by column chromatography with silica gel by using 1:1 ethyl acetate:hexane by volume (yield: 72%). ^{1}H NMR (400 MHz, DMSO-*d*): δ = 7.89 (d, 2H), 7.75 (d, 2H), 3.82 (s, 3H), 2.23 (s, 2H), 1.03 (s, 9H) ppm.

4-(3,3-dimethylbutanamido)benzoic acid (**11**): 10 M LiOH (10 mL) was added to a stirred solution of compound **12** (4.25 mmol) in ethanol (40 mL). The mixture was heated to 60°C and refluxed for 3 h, and then neutralized with an aqueous HCl solution. The precipitate was filtered off, and washed with water several times. The crude product was purified by reprecipitation from chloroform and methanol and dried under vacuum (yield: 98%). ^{1}H NMR (400 MHz, DMSO-*d*): δ = 7.87 (d, 2H), 7.72 (d, 2H), 2.23 (s, 2H), 1.03 (s, 9H) ppm.

Methyl 4-(4-(3,3-dimethylbutanamido)benzamido)benzoate (**10**): EDC (6.37 mmol), and DMAP (6.37 mmol) were added to a solution of compound **11** (2.13 mmol), and methyl 4-aminobenzoate (6.37 mmol) in dimethylformamide (30 mL). The solution was stirred for 24 h at 50 °C. After the reaction, the solvent was removed in vacuum, and the remaining residue was precipitated in water. The crude mixture was collected with filter flask. The filtered solid was washed with excess methanol and dried in vacuum (yield: 83%). ^{1}H NMR (400 MHz, DMSO-*d*): δ = 7.95 (m, 6H), 7.77 (d, 2H), 3.84 (s, 3H), 2.24 (s, 2H), 1.04 (s, 9H) ppm.

4-(4-(3,3-dimethylbutanamido)benzamido)benzoic acid (**9**): 10M LiOH (10 mL) was added to a stirred solution of compound **10** (2.55 mmol) in tetrahydrofuran (20 mL) and ethanol (10 mL). The mixture was refluxed for 6 h and then neutralized with an aqueous HCl solution. The precipitate was filtered off, washed with water, and dried under vacuum to afford the product (yield: 98%). ^{1}H NMR (400 MHz, DMSO-*d*): δ = 7.93 (m, 6H), 7.76 (d, 2H), 2.24 (s, 2H), 1.04 (s, 9H) ppm.

tert-Butyl 4-(4-(4-(3,3-dimethylbutanamido)benzamido)benzamido)phenylcarbamate (**8**): Into dimethylformamide (20 mL), compound **9** (0.85 mmol), BPP (2.55 mmol), EDC (2.55 mmol), and DMAP (2.55 mmol) were added. The well-dissolved solution was stirred at room temperature for 24 h. After solvent evaporation, the crude mixture was washed with water and methanol to give the desired white solid product (yield: 81%). ^{1}H NMR (400 MHz, DMSO-*d*): δ = 7.96 (m, 6H), 7.77 (d, 2H), 7.64 (d, 2H), 7.41 (d, 2H), 2.25 (s, 2H), 1.46 (s, 9H), 1.05 (s, 9H) ppm.

N-(4-(amino)phenyl)-4-(4-(3,3-dimethylbutanamido)benzamido)benzamide (**7**): TFA (500 μL) was added dropwise into the solution of compound **8** (0.55 mmol) in methylene chloride (15 mL). After stirring the mixture for 6 h at room temperature, the volatiles were distilled off and the remaining mixture was washed with saturated $NaHCO_3$ solution. The solid precipitate was filtered and dried in vacuum (yield: 99%). ^{1}H NMR (400 MHz, DMSO-*d*): δ = 7.95 (m, 6H), 7.75 (d, 2H), 7.48 (d, 2H), 6.72 (d, 2H), 2.25 (s, 2H), 1.05 (s, 9H) ppm.

2,2',2",2'"-((((2-((4-(4-(4-(3,3-dimethylbutanamido)benzamido)benzamido)phenyl)amino)-2-oxoethyl)azanediyl)bis(ethane-2,1-diyl))bis(azanetriyl))tetraacetate (**1**): A solution of compound **7** (0.29 mmol), DPTA (058 mmol), EDC (1.17 mmol), and DMAP (1.17 mmol) in dimethylformamide (20 mL) was stirred at 50 °C for 72 h. After the reaction, the solvent was removed in vacuum. The remaining residue was purified by flash column chromatography with silica gel by using 7:1 tetrahydrofuran : chloroform by volume as an eluent. The isolated compound was then reacted with TFA (500 μL) in methylene chloride (15 mL) for 48 h. The volatile fraction was removed under reduced pressure. Tetrahydrofuran was added to suspend the product and the product was collected by filtration (yield: 67%). ^{1}H NMR (400 MHz, DMSO-*d*): δ = 7.97 (m, 6H), 7.75 (m, 4H), 7.61 (d, 2H), 4.06 (s, 2H), 3.51 (s, 8H), 3.21 (t, 4H), 3.01 (t, 4H), 2.25 (s, 2H), 1.05 (s, 9H) ppm. ^{13}C NMR (400 MHz, DMSO-*d*): δ = 173.2, 170.9, 165.6, 165.1, 142.9, 135.7, 134.4, 128.9, 121.2, 119.8, 118.7, 55.1, 52.8, 50.1, 31.4, 30.1 ppm. MS (MALDI-ToF) m/z $[M + H]^+$ calculated: 820.34; $[M + H]^+$ found: 820.35.

S1c. Zwitterionic amphiphile and its intermediates

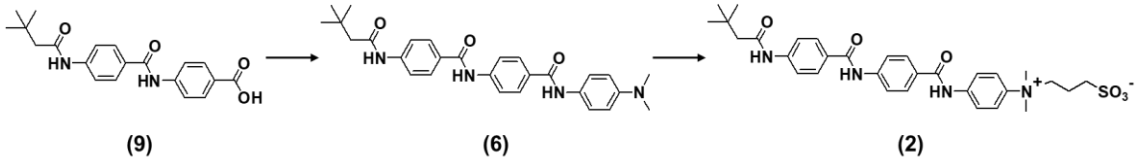

Supplementary Scheme 2. Synthesis scheme to obtain zwitterionic amphiphile.

N-(4-(dimethylamino)phenyl)-4-(4-(3,3-dimethylbutanamido)benzamido)benzamide (**6**): A solution of compound **9** (0.85 mmol), DPP (2.55 mmol), EDC (2.55 mmol), and HOBt (2.55 mmol) in

dimethylformamide (20 mL) was stirred at 50 °C for 24 h. After the reaction, the solvent was distilled off and the remaining residue was precipitated with water. The crude mixture was collected and washed with chloroform several times (yield: 78%). ^{1}H NMR (400 MHz, DMSO-*d*): δ = 7.95 (m, 6H), 7.77 (d, 2H), 7.57 (d, 2H), 6.73 (d, 2H), 2.88 (s, 6H), 2.25 (s, 2H), 1.05 (s, 9H) ppm.

3-((4-(4-(4-(3,3-dimethylbutanamido)benzamido)benzamido)phenyl)dimethylammonio)-propane -1-sulfonate (**2**): Compound **6** (1.85 mmol) was dissolved in dimethylformamide (15 mL) and tetrahydrofuran (15 mL). PPS (5 mL) was slowly injected using a syringe and the clear solution was stirred for 48 h in a sealed pressure tube at 70 °C. The volatile fraction was removed under reduced pressure and acetonitrile (50 mL) was added. The resulting precipitate was filtered and dried in vacuum (yield: 85%). ^{1}H NMR (400 MHz, DMSO-*d*): δ = 7.98 (m, 8H), 7.90 (d, 2H), 7.78 (d, 2H), 3.99 (m, 2H), 3.58 (s, 6H), 2.39 (t, 2H), 1.66 (m, 2H), 1.05 (s, 9H) ppm. ^{13}C NMR (400 MHz, DMSO-*d*): δ = 170.9, 165.8, 143.2, 140.9, 139.6, 129.1, 122.2, 121.1, 119.8, 118.7, 68.1, 54.4, 50.1, 47.9, 34.4, 30.1, 20.3 ppm. MS (MALDI-ToF) $[M + H]^+$ m/z calculated: 595.26; $[M + H]^+$ found: 595.41.

S1d. Cationic amphiphile and its intermediates

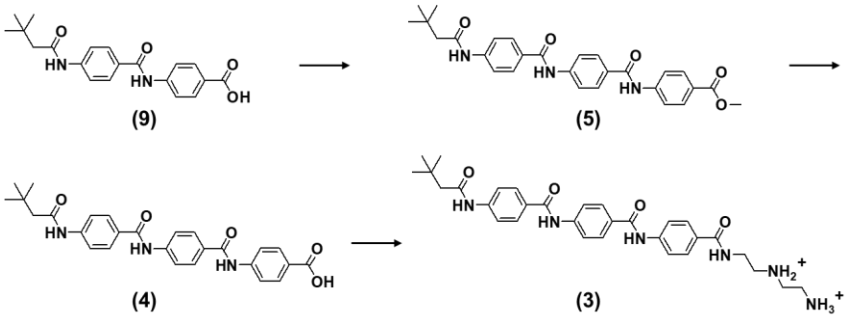

Supplementary Scheme 3. Synthesis scheme to obtain the cationic amphiphile.

Methyl 4-(4-(4-(3,3-dimethylbutanamido)benzamido)benzamido)benzoate (**5**): EDC (4.23 mmol) and DMAP (4.23 mmol) were added to a solution of compound **9** (1.41 mmol) and methyl 4-aminobenzoate (4.23 mmol) in dimethylformamide (20 mL). The solution was stirred for 24 h at 50 °C. After the reaction, the solvent was removed in vacuum, and the remaining residue was precipitated with water. The collected crude mixture was further washed with methanol and dried in vacuum (yield: 75%). ^{1}H NMR (400 MHz, DMSO-*d*): δ = 7.97 (m, 8H), 7.78 (d, 2H), 3.85 (s, 3H), 2.25 (s, 2H), 1.05 (s, 9H) ppm.

4-(4-(4-(3,3-dimethylbutanamido)benzamido)benzamido)benzoic acid (**4**): 10M LiOH (10 mL) was added to a stirred solution of compound **5** (1.05 mmol) in tetrahydrofuran (20 mL), and ethanol (10 mL). The mixture was refluxed for 12 h and then neutralized with an aqueous HCl solution to obtain a precipitate. The crude product was purified by reprecipitation with chloroform and ethanol and dried under vacuum (yield: 93%). ^{1}H NMR (400 MHz, DMSO-*d*): δ = 7.94 (m, 8H), 7.78 (d, 2H), 2.25 (s, 2H), 1.05 (s, 9H) ppm.

1-(2-(4-(4-(4-(3,3-dimethylbutanamido)benzamido)benzamido)benzamido)ethyl)ethane-1,2-diaminium (**3**): A solution of compound **4** (0.42 mmol), BBT (1.27 mmol), EDC (1.27 mmol), HOBt (1.27 mmol) and DIPEA (1.27 mmol) in dimethylformamide (20 mL) and dichloromethane (20 mL) was stirred at room temperature for 24 h. After the reaction, the solvent was removed in vacuum, and the remaining residue was washed with water several times. The isolated compound was then reacted with TFA (4 mL) in methylene chloride (40 mL) for 24 h. The volatile fraction was evaporated under reduced pressure. Diethyl ether was added to collect the product by filtration (yield: 85%). ^{1}H NMR (400 MHz, DMSO-*d*): δ = 7.98

(m, 10H), 7.76 (d, 2H), 3.58 (m, 2H), 3.39 (m, 2H), 3.13 (m, 4H), 2.25 (s, 2H), 1.04 (s, 9H) ppm. ^{13}C NMR (400 MHz, DMSO-*d*): δ = 171.1, 167.1, 165.7, 142.9, 129.1, 128.7, 128.4, 120.1, 119.4, 118.7, 50.1, 47.4, 44.6, 35.8, 31.4, 30.1 ppm. MS (MALDI-ToF) $[M + H]^+$ m/z calculated: 559.30; $[M + H]^+$ found: 559.29.

S1e. Synthesis of materials for Förster resonance energy transfer

Molecular exchange was measured by Förster resonance energy transfer (FRET) dark quenching when two nanoribbon populations, one containing a donor fluorophore and the other containing a dark quencher, were introduced into the same suspension. EDANS ((5-((2-aminoethyl)amino)naphthalene-1-sulfonic acid)) was used as the donor fluorophore and DABCYL (4-(dimethylaminoazo)benzene-4-carboxylic acid) was used as the dark quencher.

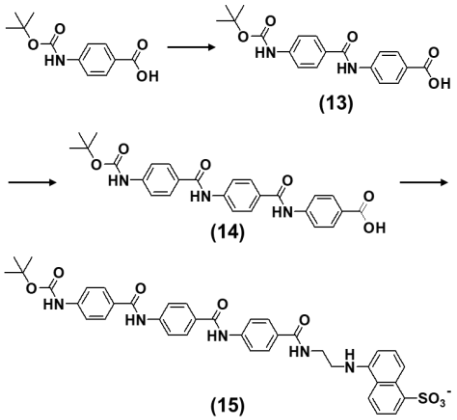

Supplementary Scheme 4. Synthesis scheme to obtain the EDANS-tagged amphiphile.

4-(4-(*tert*-Butoxycarbonyl)benzamido)benzoic acid (**13**): A solution of 4-(Boc-amino)benzoic acid (4.21 mmol), methyl 4-aminobenzoate (8.42 mmol), EDC (8.42 mmol), and DMAP (8.42 mmol) in chloroform (100 mL) were stirred at room temperature for 12 h. After the reaction, the solvent was evaporated under reduced pressure, and the remaining residue was precipitated with water. The mixture was filtered, and the precipitate was washed with methylene chloride several times. The solid material was dissolved in tetrahydrofuran (40 mL) and ethanol (20 mL). LiOH (21.1 mmol) in water (10 mL) was added to this solution, which was then refluxed at 70 °C for 3 h. The reaction mixture was shifted to room temperature and acidified to pH 2 with the addition of 5M HCl solution. The precipitate was collected by filtration and dried in vacuum (yield: 87%). ^{1}H NMR (400 MHz, DMSO-*d*): δ = 7.93 (m, 6H), 7.66 (d, 2H), 1.49 (s, 9H) ppm.

4-(4-(4-(*tert*-Butoxycarbonyl)benzamido)benzamido)benzoic acid (**14**): A solution of compound **13** (2.11 mmol), methyl 4-aminobenzoate (4.22 mmol), EDC (4.22 mmol), and DMAP (4.22 mmol) were in dimethylformamide (30 mL) was stirred at room temperature for 24 h. After the reaction, the solvent was distilled off, and the remaining residue was washed with water and methanol. The solid material was dissolved in tetrahydrofuran (20 mL) and ethanol (10 mL). LiOH (10.5 mmol) in water (10 mL) was added to this solution, which was then refluxed at 70 °C for 6 h. The reaction mixture was shifted to room temperature and acidified to pH 2 with the addition of 5M HCl solution. The precipitate was collected by filtration and dried in vacuum (yield: 82%). ^{1}H NMR (400 MHz, DMSO-*d*): δ = 7.95 (m, 10H), 7.67 (d, 2H), 1.49 (s, 9H) ppm.

EDANS-tagged amphiphile, 5-((2-(4-(4-(4-(3,3-dimethylbutanamido)benzamido)benzamido) benzamido)ethyl)amino)naphthalene-1-sulfonic acid (**15**): A solution of compound **14** (0.21 mmol), EDC (0.25 mmol), and DMAP (0.25 mmol) in dimethylformamide (10 mL) was stirred for 30 min. EDANS (0.25 mmol) was then added into the solution and the solution was stirred for 24 h at room temperature. Water

was poured into the solution to yield a precipitate, which was obtained by filtration and washed with chloroform (yield: 64%). ^{1}H NMR (400 MHz, DMSO-*d*): δ = 8.02 (m, 1H), 7.97 (m, 10H), 7.62 (d, 2H), 7.34 (m, 4H), 6.57 (d, 1H), 3.85 (m, 1H), 3.43 (m, 2H), 3.16 (m, 2H), 1.51 (s, 9H) ppm. MS (MALDI-ToF) $[M + H]^+$ m/z calculated: 723.23; $[M + H]^+$ found: 723.24.

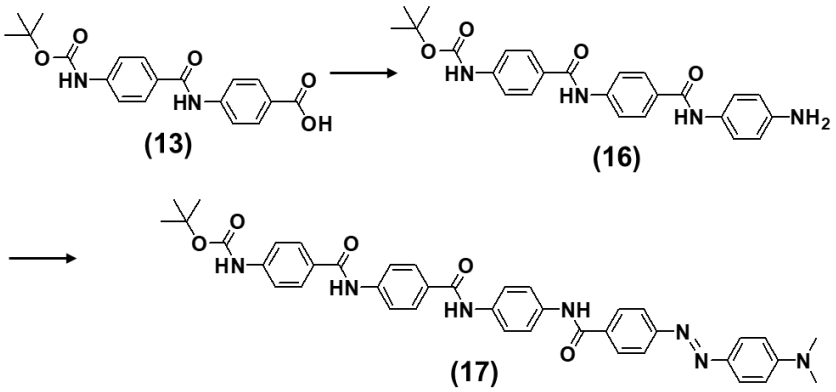

Supplementary Scheme 5. Synthesis scheme to obtain the DABCYL-tagged amphiphile.

tert-Butyl 4-((4-((4-aminophenyl)carbamoyl)phenyl)carbamoyl)phenylcarbamate (**16**): A solution of compound **13** (0.56 mmol), 1,4-diaminobenzene (11.22 mmol), EDC (0.67 mmol), and DMAP (0.67 mmol) in dimethylformamide (80 mL) was stirred at 25 °C for 24 h. The volatile fraction was removed under reduced pressure and the remaining residues were washed several times with methanol and filtered to obtain the product (yield: 59%). ^{1}H NMR (400 MHz, DMSO-*d*): δ = 7.92 (m, 6H), 7.60 (d, 2H), 7.36 (d, 2H), 6.54 (d, 2H), 4.91 (s, 2H), 1.51 (s, 9H) ppm.

DABCYL-tagged amphiphile, (E)-4-((4-(dimethylamino)phenyl)diazenyl)-N-(4-(4-(4-(3,3-dimethylbutanamido)benzamido)benzamido)phenyl)benzamide (**17**): A solution of compound **16** (0.67 mmol), DABCYL (0.81 mmol), EDC (0.81 mmol), and DMAP (0.81 mmol) in dimethylformamide (10 mL) was stirred at 25 °C for 48 h. The solvent was then evaporated under reduced pressure. The crude mixtures were purified with water and chloroform and filtered to obtain the product (yield: 71%). ^{1}H NMR (400 MHz, DMSO-*d*): δ = 7.94 (m, 12H), 7.62 (d, 4H), 7.45 (d, 2H), 6.66 (d, 2H), 3.10 (s, 6H), 1.51 (s, 9H) ppm. MS (MALDI-ToF) $[M + Na]^+$ m/z calculated: 720.29; $[M + Na]^+$ found: 720.30.

S1f. Oligo(ethylene glycol) amphiphile

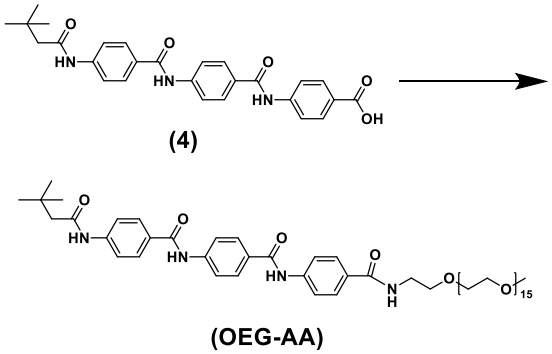

Supplementary Scheme 6. Synthesis scheme to obtain the oligo(ethylene glycol) amphiphile.

N-(4-((2,5,8,11,14,17,20,23,26,29,32,35,38,41,44,47-hexadecaoxanonatetracontan-49-yl)carbamoyl)phenyl)-4-(4-(3,3-dimethylbutanamido)benzamido)benzamide (**OEG-AA**): A solution of compound **4** (0.1 mmol), methoxypolyethylene glycol amine (M_w = 750 g/mol, 0.2 mmol), EDC (0.2 mmol), and HOBt (0.2 mmol) in dimethylformamide (10 mL) was stirred at rt for 24 h. The solvent was then evaporated under reduced pressure and the remaining residue was dissolved in dichloromethane. The solution was washed by ice water twice via solvent extraction and the organic fraction in dichloromethane was retained. The final product in dichloromethane was obtained by removing the solvent under reduced pressure and lyophilizing the remaining semi-solid (yield: 62%). ^{1}H NMR (400 MHz, DMSO-*d*): δ = 7.97 (m, 6H), 7.84 (m, 2H), 7.76 (d, 2H), 7.49 (d, 2H), 3.51 (s, 70H), 2.25 (m, 2H), 1.05 (s, 9H) ppm.
Major peak: MS (MALDI-ToF) $[M + Na]^+$ m/z calculated for n = 15 is 1213.64; $[M + Na]^+$ Found: 1213.61
Minor peak: MS (MALDI-ToF) $[M + Na]^+$ m/z calculated for n = 13 is 1125.58; $[M + Na]^+$ Found: 1125.56
Minor peak: MS (MALDI-ToF) $[M + Na]^+$ m/z calculated for n = 14 is 1169.61; $[M + Na]^+$ Found: 1169.59
Minor peak: MS (MALDI-ToF) $[M + Na]^+$ m/z calculated for n = 16 is 1257.66; $[M + Na]^+$ Found: 1257.64
Minor peak: MS (MALDI-ToF) $[M + Na]^+$ m/z calculated for n = 17 is 1301.69; $[M + Na]^+$ Found: 1301.67

S2. Chemical characterization

S2a. Nuclear magnetic resonance

Proton (^{1}H) and carbon (^{13}C) nuclear magnetic resonance (NMR) measurements were performed on a Bruker Avance III DPX 400. 20 mg of sample were dissolved in 500 µL deuterated dimethylsulfoxide (DMSO-*d*) for analysis. The chemical shifts were measured in parts per million (ppm) down-field from tetramethylsilane. Self-assembly behavior was also modulated and studied by addition of deuterated water to the DMSO-*d* solutions, as discussed with Supplementary Figs. 16-18.

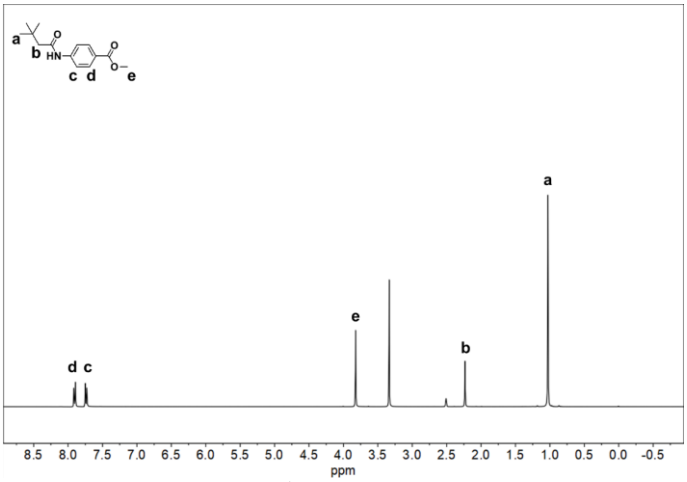

Supplementary Fig. 1. ^{1}H NMR spectra of compound **12**.

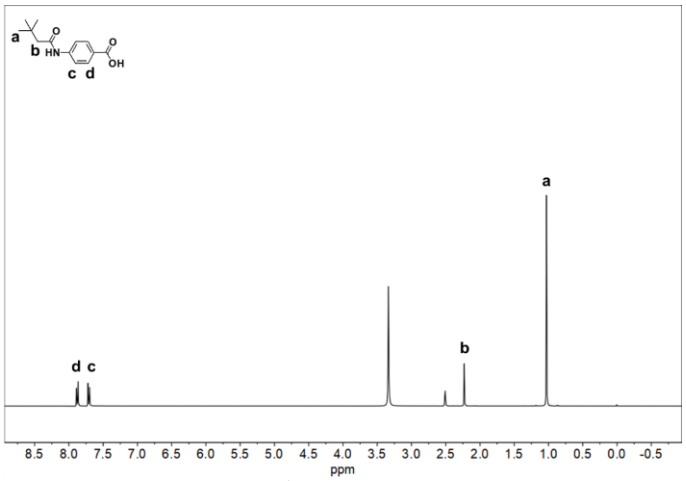

Supplementary Fig. 2. ^{1}H NMR spectra of compound **11**.

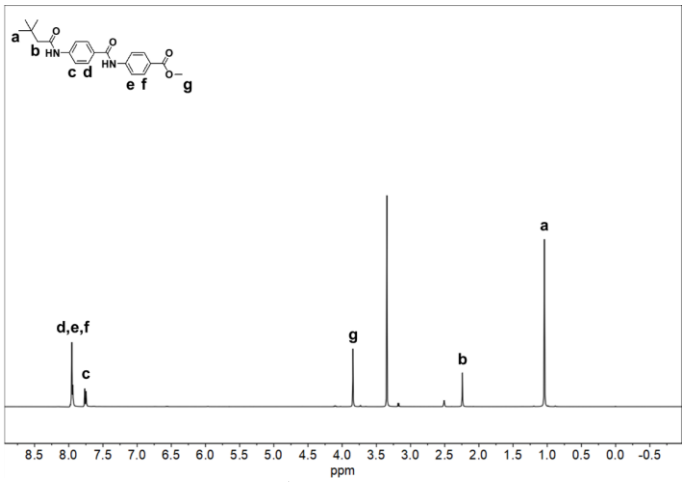

Supplementary Fig. 3. ^{1}H NMR spectra of compound **10**.

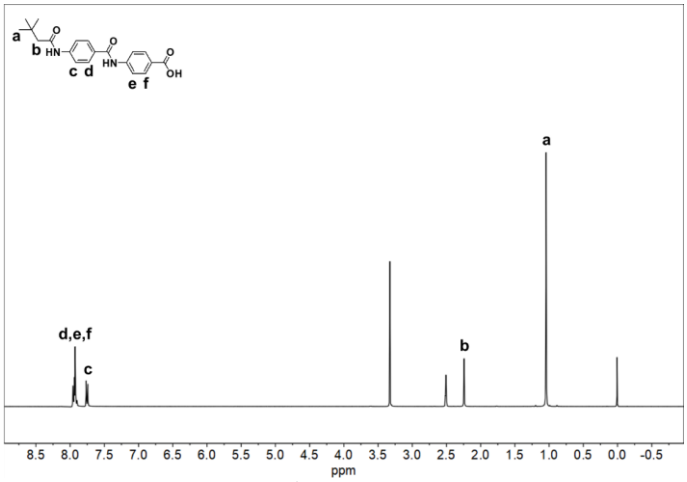

Supplementary Fig. 4. ^{1}H NMR spectra of compound **9**.

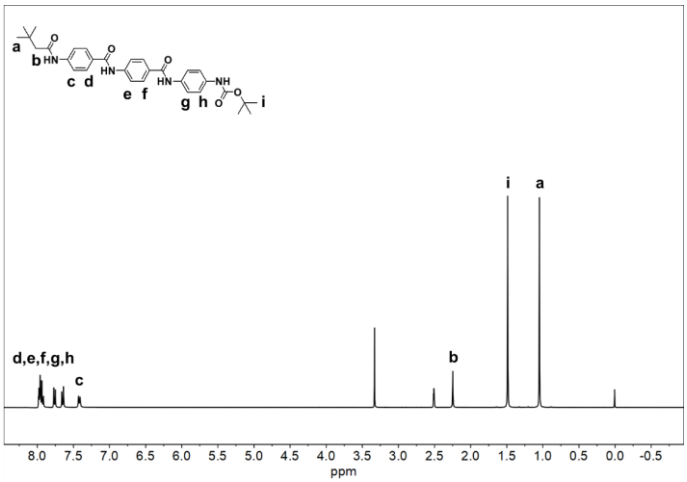

Supplementary Fig. 5. ^{1}H NMR spectra of compound **8**.

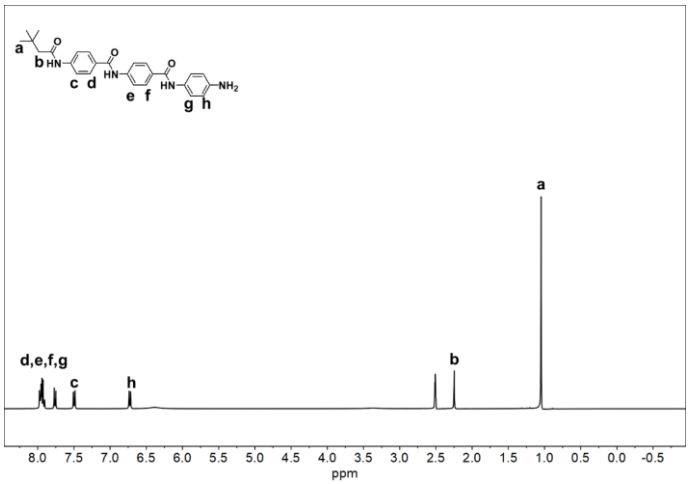

Supplementary Fig. 6. ^{1}H NMR spectra of compound **7**.

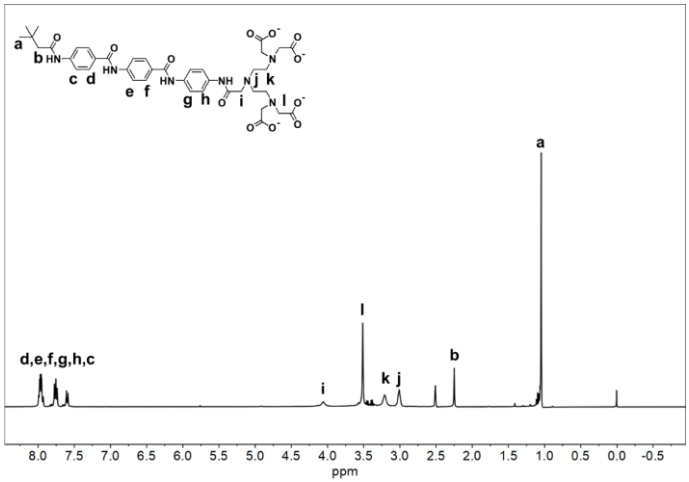

Supplementary Fig. 7. ^{1}H NMR spectra of compound **1**.

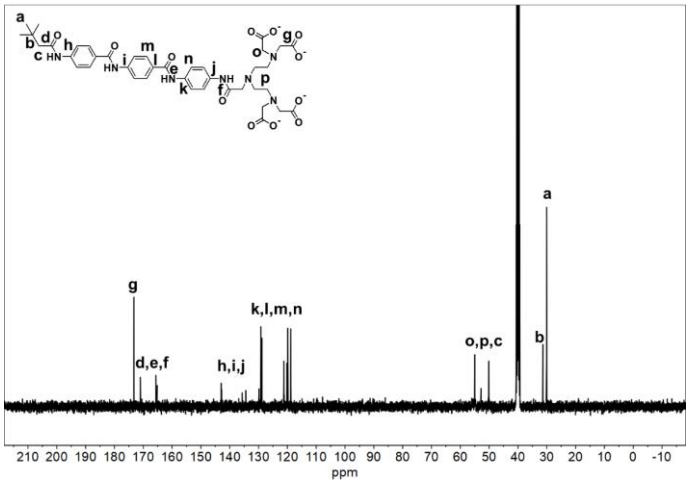

Supplementary Fig. 8. ^{13}C NMR spectra of compound **1**.

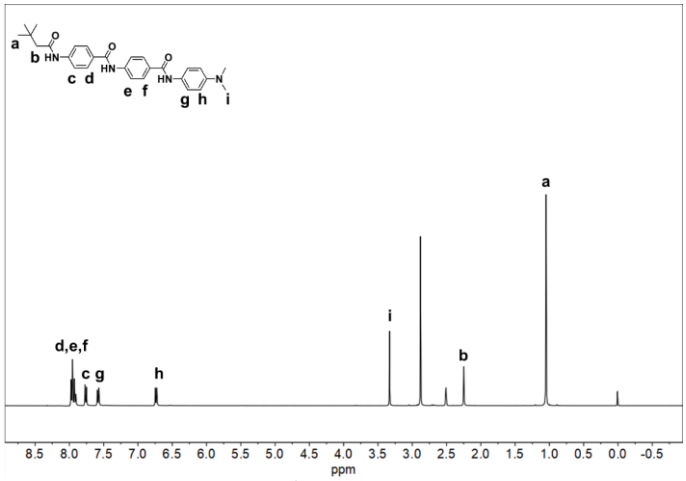

Supplementary Fig. 9. ^{1}H NMR spectra of compound **6**.

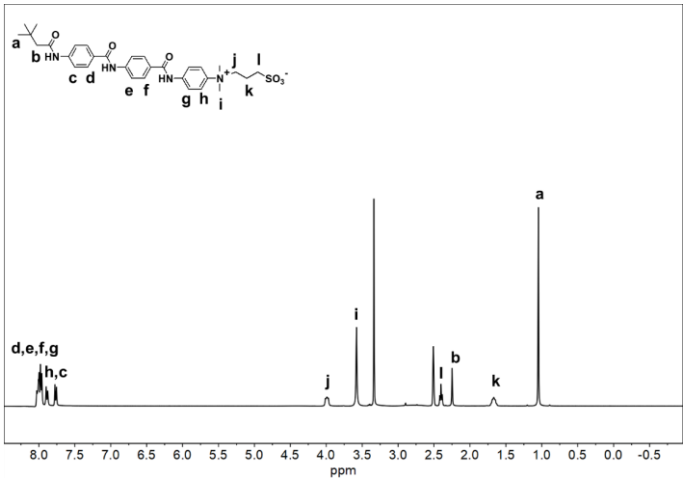

Supplementary Fig. 10. ^{1}H NMR spectra of compound **2**.

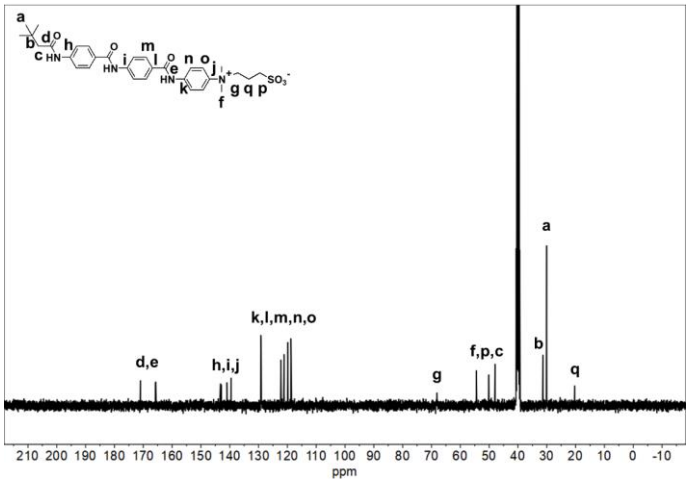

Supplementary Fig. 11. ^{13}C NMR spectra of compound **2**.

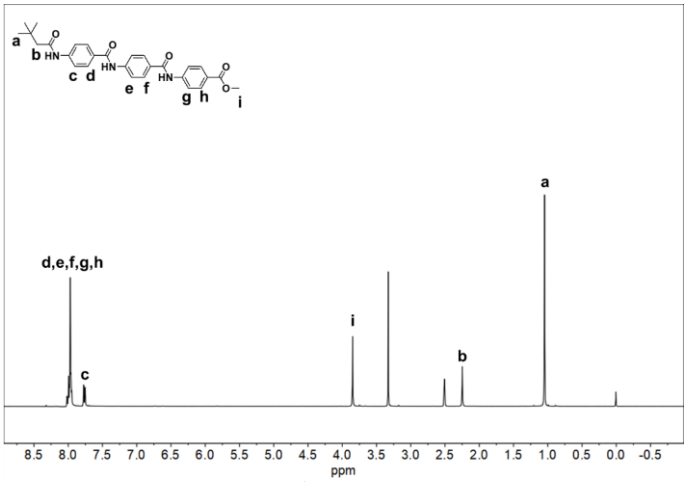

Supplementary Fig. 12. ^{1}H NMR spectra of compound **5**.

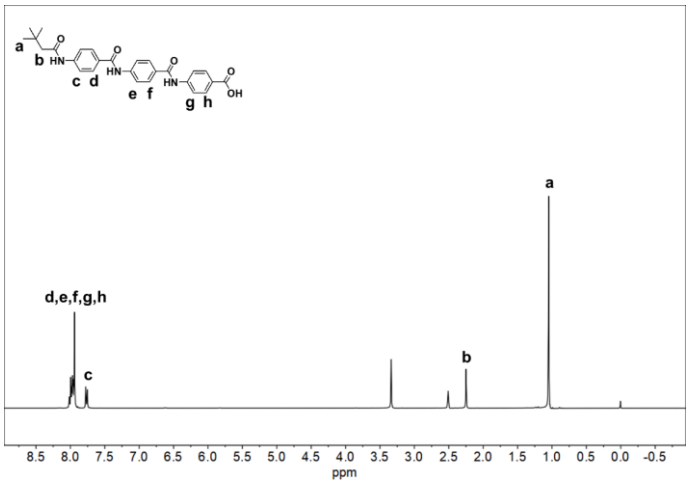

Supplementary Fig. 13. ^{1}H NMR spectra of compound **4**.

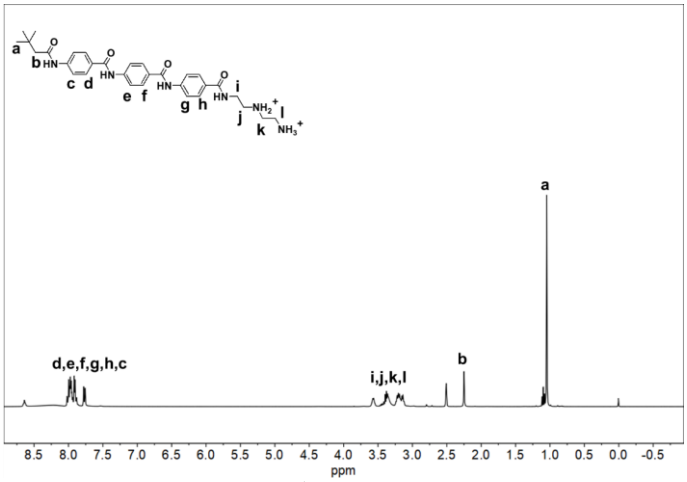

Supplementary Fig. 14. ^{1}H NMR spectra of compound **3**.

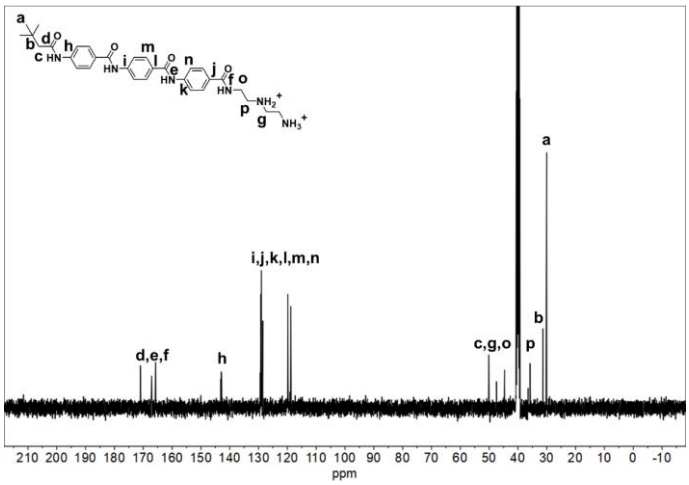

Supplementary Fig. 15. ^{13}C NMR spectra of compound **3**.

Solvent effects: The self-assembly behavior of aramid amphiphiles can be mediated by solvent variation as shown in Supplementary Figs. 16-18. In good solvent, such as DMSO-*d*, the ^{1}H NMR spectrum of aramid amphiphile samples indicate a monomeric state with well-resolved sharp peaks corresponding to aromatic protons between δ = 8.1 and 7.5 ppm. The aromatic proton peaks broaden as aggregation occurs when D_2O is titrated into the solution. The broadening of the aromatic H_1 and H_2 peaks is concomitant with the formation of strong intermolecular interactions upon self-assembly. The simultaneous upfield shift of protons is observed when small intermolecular distances induce a magnetic shielding effect. The broadening of the aromatic proton peaks is consistent with slowing of conformational dynamics within the nanostructures as assembly occurs with increasing D_2O concentrations. Compound **3** exhibits enhanced NMR signal at higher D_2O concentrations due to its higher solubility in D_2O than compounds **1** and **2**. No nanoribbons or other assemblies of compound **3** are observed in conventional TEM when a grid is prepared from the sample of 100% DMSO-*d*.

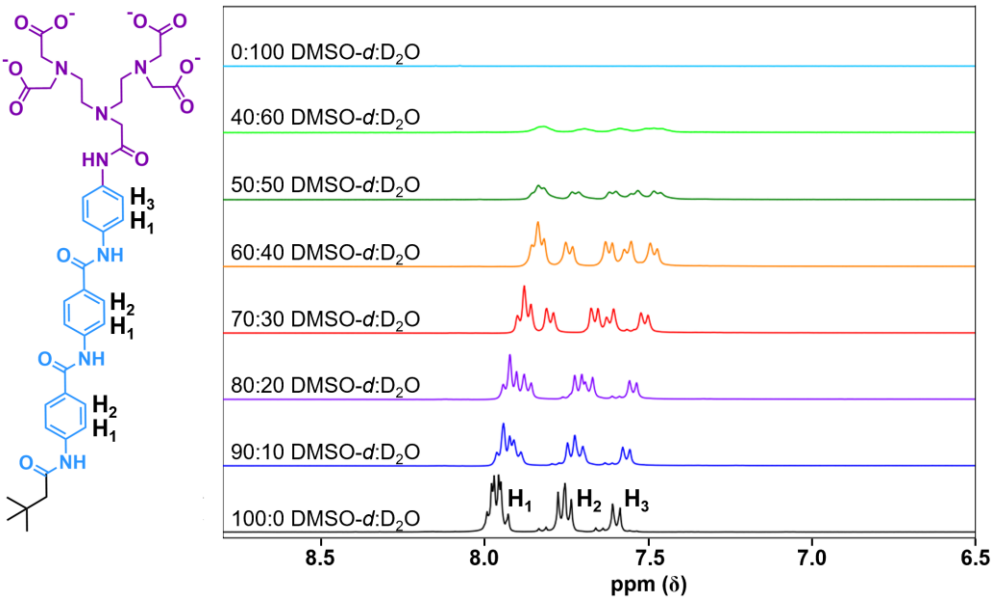

Supplementary Fig. 16. ^{1}H NMR spectra of compound **1** in DMSO-*d* with increasing D_2O content.

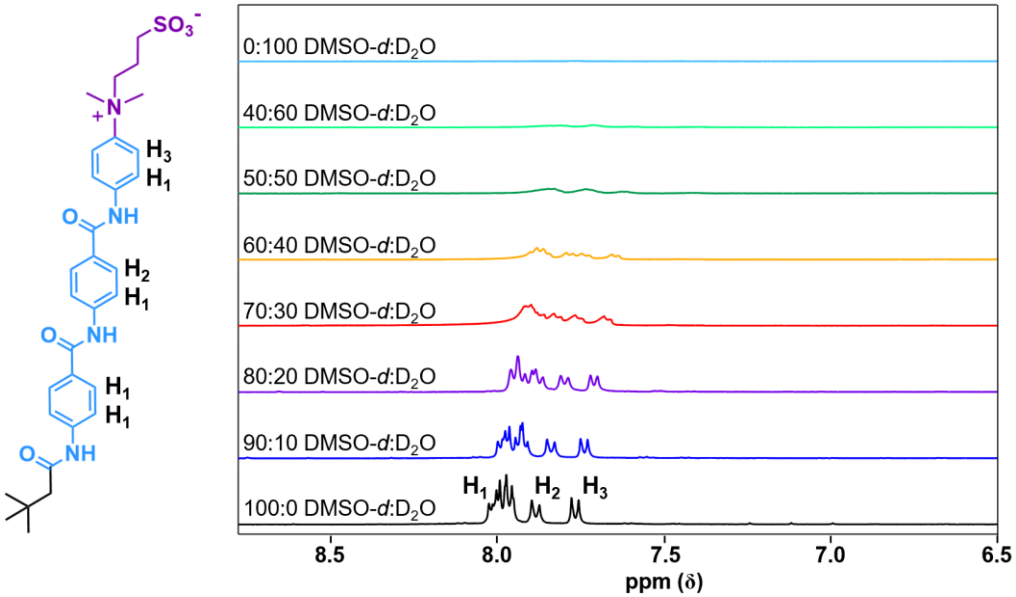

Supplementary Fig. 17. ^{1}H NMR spectra of compound **2** in DMSO-*d* with increasing D_2O content.

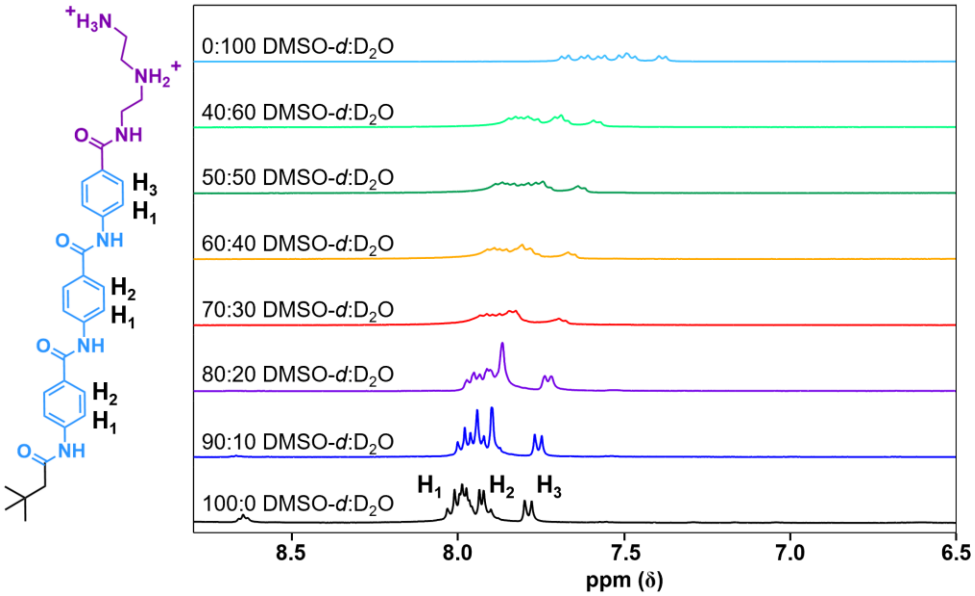

Supplementary Fig. 18. ^{1}H NMR spectra of compound **3** in DMSO-*d* with increasing D_2O content.

S2b. Mass spectrometry

Molecular weights of amphiphiles were determined using a Bruker Omniflex matrix assisted laser desorption/ionization-time-of-flight (MALDI-ToF) instrument with a Reflectron accessory. A matrix solution was prepared by adding 15 mg of *α*-cyano-4-hydroxycinnamic acid to 1 mL of 1:1 water:acetonitrile by volume with 0.1% TFA, vortexing for one minute, centrifuging for 20 s, and retaining the supernatant. 10 µL of 1 mg/mL amphiphile in water was then transferred into a centrifuge tube and diluted with the matrix solution to a 50 pmol/µL concentration. 1 µL of a 1 mg/mL calibrant solution (SpheriCal Peptide Low, Polymer Factory) in tetrahydrofuran was added to the solutions as an internal calibrant. 2 µL of each mass spectrometry solution was pipetted and dried onto a sample plate for analysis.

S2c. Attenuated total reflectance Fourier-transform infrared spectroscopy

ATR-FTIR spectra of compound **3** were captured across systematically varying concentrations of DMSO-*d* and D_2O to characterize hydrogen bonding between amphiphiles. The results of this study with powder control samples of compound **3** and compound **4**, a synthesis intermediate with no head group, are shown in Supplementary Fig. 19.

Characteristic β-sheet hydrogen bonding is commonly investigated via amide I vibration shifting around 1650 cm^{-1}.[37] Two peaks are observed in this region at 1672 and 1652 cm^{-1} for the compound **3** powder (unassembled) sample. The peak at 1672 cm^{-1} is not observed for compound **4**, which lacks the amide bond that couples the amphiphile head group to the aramid structural domain. Therefore, we assign the peak at 1672 cm^{-1} to the C = O stretch of the amide bond between the head group and structural domain and 1652 cm^{-1} to the C = O stretch of the amide bonding in aramid structural domain. We observe the peak at 1672 cm^{-1} is present among all mixtures of DMSO-*d* and D_2O. Conversely, the amide I peak shifts to 1638 cm^{-1} in the full D_2O environment. This red shift indicates hydrogen bonding formation between at the corresponding amide bonding when compound **3** assembles in D_2O.[38] The peak at 1600 cm^{-1} is attributed to C – C stretching in the aromatic rings and is constant over all spectra.

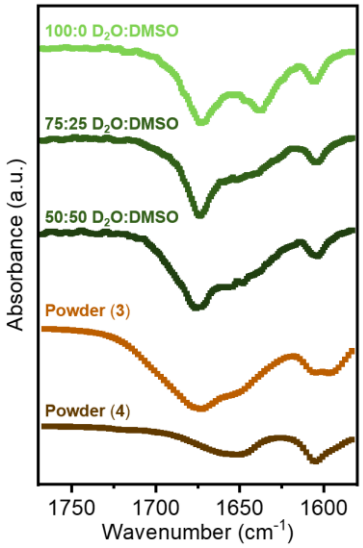

Supplementary Fig. 19. FTIR spectra of compounds **3** and **4** in dried powder form as controls and compound 3 dissolved in varying ratios of DMSO-*d* to D_2O.

Supplementary Fig. 20 shows the effect of bath sonication time on ATR-IR spectra of compound **3** dissolved in different solvent mixtures of DMSO-*d* and D_2O. Broadly, the peak at 1638 cm^{-1} is enhanced with longer sonication times and lower levels of DMSO-*d*. We attribute this sharpening to increasing uniformity of intermolecular hydrogen bonding distances upon sonication.

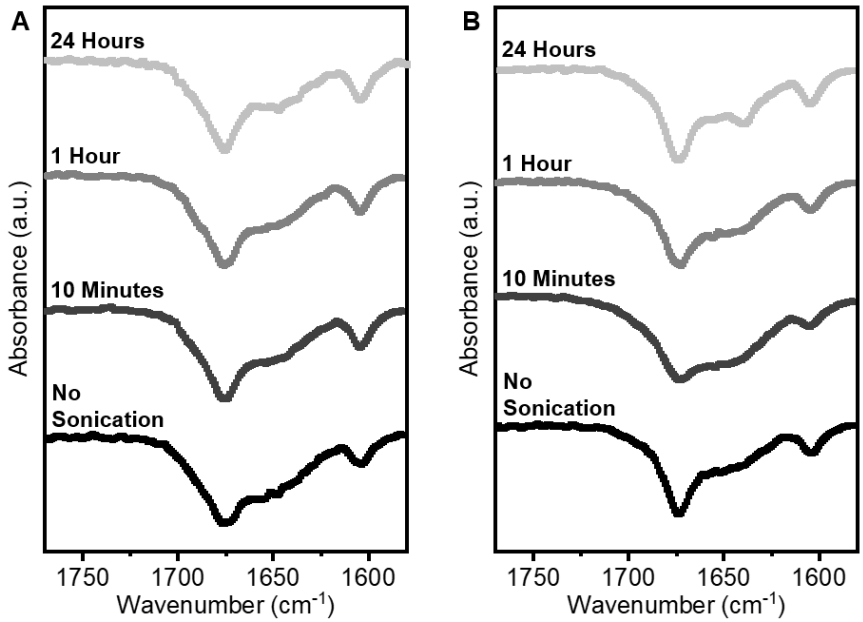

Supplementary Fig. 20. ATR-IR spectra showing the effect of sonication time on intermolecular interactions between compound **3** in (**A**) a 50:50 mixture of D_2O:DMSO-*d* and (**B**) a 75:25 mixture of D_2O:DMSO-*d*. The amide I bond at 1638 cm^{-1} is enhanced with higher proportions of water and longer sonication times, resulting from the formation of a more uniform hydrogen bonding network in the self-assembled system.

S3. Structural characterization

S3a. Transmission electron microscopy

Conventional transmission electron microscopy (TEM) of nanoribbons formed by self-assembly of **1**, **2**, and **3** are shown in Supplementary Fig. 21.

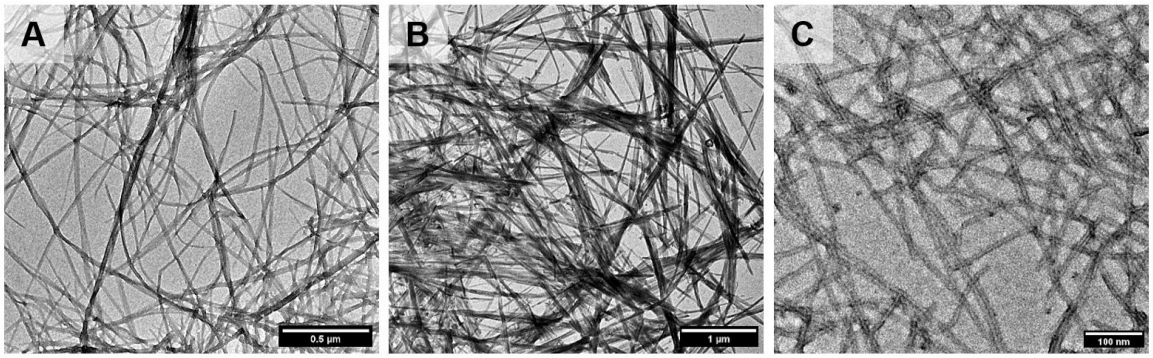

Supplementary Fig. 21. TEM images of assemblies of compounds (**A**) **1**, (**B**) **2**, and (**C**) **3**.

Changing the environment pH can modulate assembly morphology by changing the effective head group charge and size of amphiphiles. Aqueous suspensions of compounds **1**, **2**, and **3** at 0.1 mg/mL concentrations were adjusted to pH 3 and pH 11 using 0.5 M hydrochloric acid and sodium hydroxide, respectively, and bench sonicated for 10 minutes to investigate the effect of pH on assembly morphology. Compound **1** forms disordered aggregates at pH 3 and short noodle-like assemblies at pH 11; compound **2** forms needle-like assemblies at pH 3 and disordered aggregates at pH 11; and compound **3** forms cylindrical nanotubes at pH 3 and plate-like aggregates at pH 11. Representative micrographs showing these structures are shown in Supplementary Fig. 22.

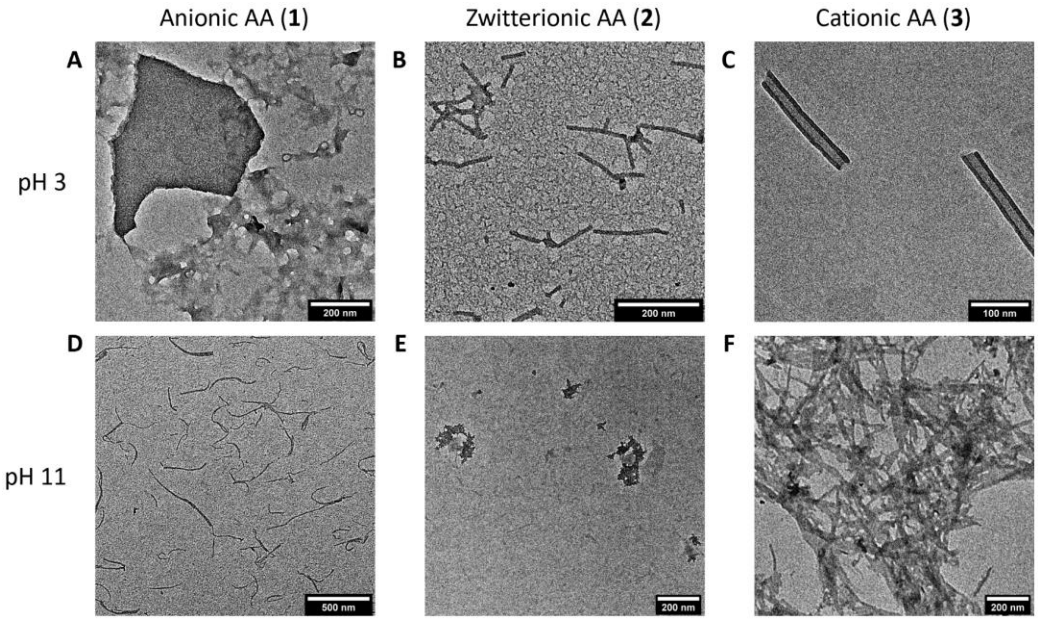

Supplementary Fig. 22. The self-assembly morphology of aramid amphiphiles can be modulated by changing the pH. Representative micrographs of (**A**) compound **1** at pH 3, (**B**) compound **2** at pH 3, (C) compound **3** at pH 3, (**D**) compound **1** at pH 11, (**E**) compound **2** at pH 11, and (**F**) compound **3** at pH 11 are shown here.

S3b. Cryogenic transmission electron microscopy

Supplementary Fig. 23 shows cryo-TEM micrographs of nanoribbons of compounds **1**, **2**, and **3**, respectively. Fig. 23a shows that bundling of **1** occurs, likely due to inter-ribbon hydrogen bonding of the head groups. Interestingly, self-assembly of **2** leads to both high-aspect-ratio nanoribbons and in some cases, complete nanoribbon circles. Nanoribbon widths in Cryo-TEM for **1**, **2**, and **3** nanoribbons are measured as 5.5 nm, 5.1 nm, and 5.8 nm, respectively for n = 25 measurements with approximately 5% error.

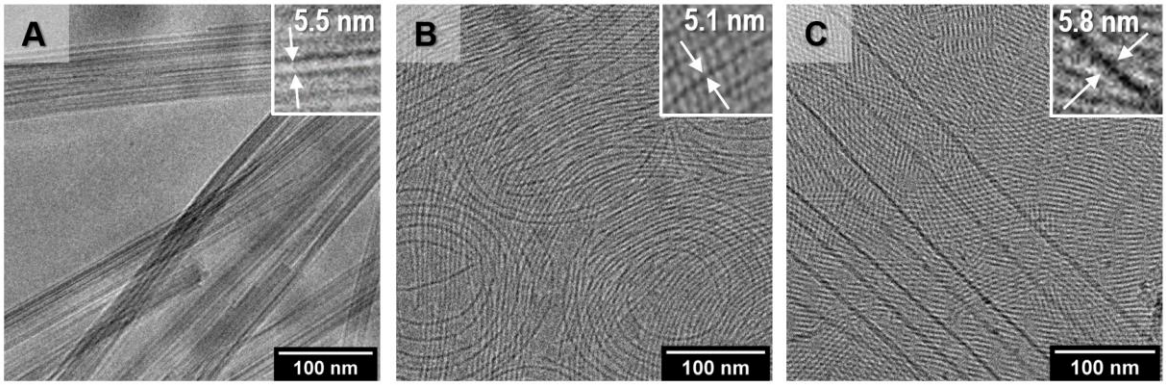

Supplementary Fig. 23. Cryo-TEM images of assemblies of compounds (**A**) **1**, (**B**) **2**, and (**C**) **3**.

Supplementary Fig. 24 shows cryo-TEM micrographs of an aramid amphiphile (OEG-AA) with an oligo(ethylene glycol) head group. The amphiphile spontaneously forms nanoribbons in water with 7.0 nm widths, 4.0 nm thickness, and lengths exceeding several micrometers. Both width and edge views are observed in Supplementary Fig. 24.

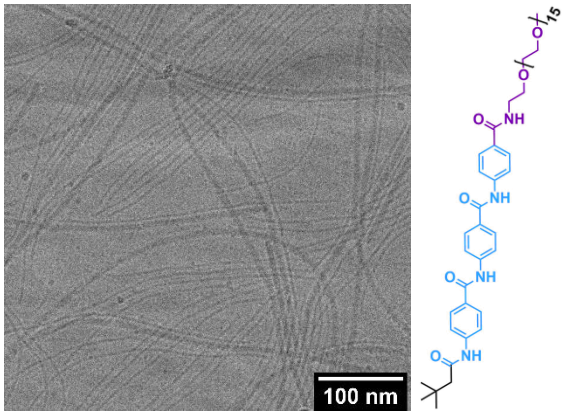

Supplementary Fig. 24. Representative Cryo-TEM image of an aramid amphiphile with a 15-mer oligo(ethylene glycol) head group, OEG-AA.

S3c. X-ray scattering

SAXS profiles of AA nanoribbons best fit to a core-shell lamellar model, which describes a lyotropic lamellar phase with head and tail group domains of different scattering length densities (SLDs).[28,29] Estimates for the SLDs of the hydrated hydrophilic head group domain (9.40×10^{-6} Å^{-2}) and the aramid-containing hydrophobic domain (11.13×10^{-6} Å^{-2}) were calculated based on the molecular formulae and input into SasView software. The solvent SLD (water) is 9.44×10^{-6} Å^{-2}. The model was adjusted to the appropriate scale and background, and fit for thickness of the two domains. The following models were

also attempted for fitting: lamellar, cylinder, flexible cylinder, core-shell cylinder*, parallelepiped, and core-shell parallelepiped*. Fits marked with an asterisk (*) allow for differing SLDs between the head and tail group domains. Despite a careful consideration of input parameters, each of these models, other than the lamellar model, fit to non-physical geometries based on Cryo-TEM images of the AA nanoribbons. In addition to the geometry of the amphiphilic nanostructures, the SAXS line shape can be affected by nanostructure aggregation, concentration, orientation/alignment, and dispersity, and instrument resolution. However, we still find this fitting useful as an indication of nanostructure geometry, complementary to other characterization techniques. From this fitting, the hydrophobic core was found to be 2.8 ± 0.1 nm and the combined hydrophilic head group thickness was found to be 1.1 ± 0.4 nm, for a total bilayer thickness of 3.9 ± 0.5 nm. The higher error in the hydrophilic region is likely due to its similar SLD as the solvent. The lamellar fits shown in Figure 2 and Supplementary Fig. 25 support that the nanoribbons adopt a rectangular cross-section as schematically illustrated in Figure 1, surrounded by a flexible, hydrated head group domain.

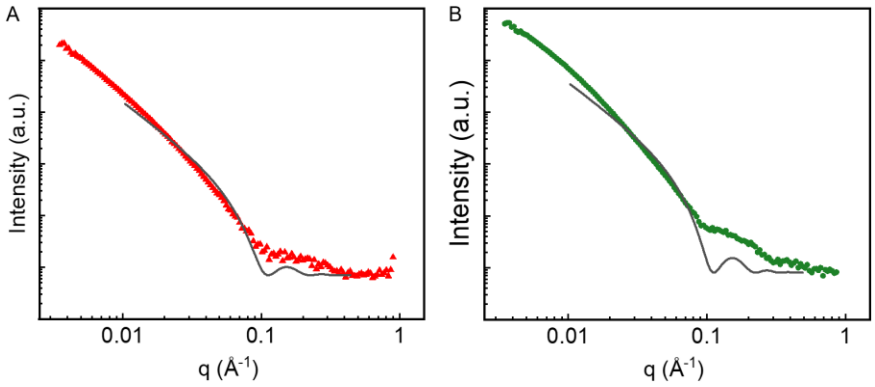

Supplementary Fig. 25. Lamellar fits (gray lines) to aqueous SAXS of (**A**) compound **1** (in red) and (**B**) compound **2** (in green) designates bilayer thicknesses of 3.9 nm for each nanoribbon.

SAXS of all aramid amphiphile assemblies was captured at 80 °C to probe the thermal stability of the nanostructures. Capillaries were heated from room temperature to 80 °C at 10 °C/min in a Linkam TMS600 heating stage and synchrotron SAXS profiles were captured at 0 min., 5 min., and 10 min. after reaching 80 °C. No changes in assembly morphology were observed under these conditions, as shown in Supplementary Fig. 26. All profiles are background subtracted using a water-filled capillary which underwent the same heating. The lower signal-to-noise observed in SAXS of compounds **1** and **2**, compared to compound **3**, is due to their limited solubility.

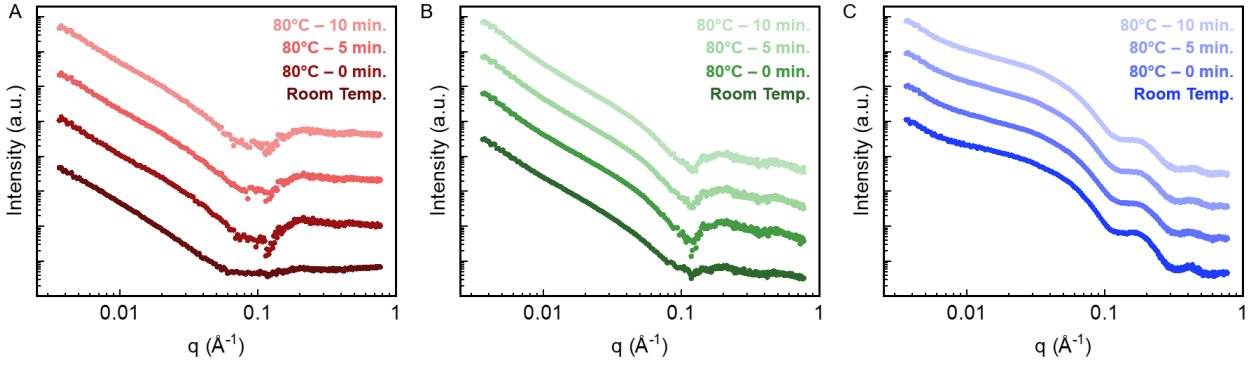

Supplementary Fig. 26. Aqueous SAXS of (**A**) compound **1**, (**B**) compound **2**, and (**C**) compound **3** shows no change in nanostructure morphology upon heating to and equilibrating at 80 °C. The significantly higher solubility of compound **3** results in SAXS profiles with stronger signal than compounds **1** and **2**.

VESTA software was used for simulating the X-ray diffraction peaks shows in Figure 5c. In this simulation, the space group 26: *P*mc2$_1$ of poly(*p*-benzamide) is considered as the most relative packing structure in aramid nanoribbons due to the constraint of the parallel amide bonding from the tri-aramid domain[34]. Further, reversing of the intensities for the two most significant peaks is observed when the thread is tilted on the X-ray beam axis. This observation indicates the two significant peaks correspond to orthogonal planes with a common intersection along the thread direction, and the assumption of the space group is confirmed. The black dotted lines of simulated peak position in Figure 5c and Supplementary Fig. 27 are generated from the unit cell with a = 7.22 Å, b = 5.05 Å and c = 11.10 Å parameters.

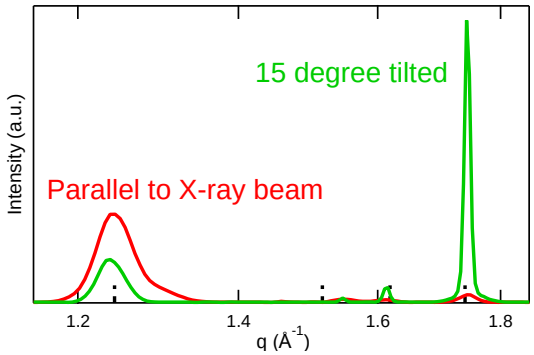

Supplementary Fig. 27. 1D-WAXS scattering profile of meridional axis with tilting on the X-ray beam direction.

S3d. Atomic force microscopy

Atomic force microscopy (AFM) of compound **3** nanoribbons deposited onto a mica substrate is shown in Supplementary Fig. 28.

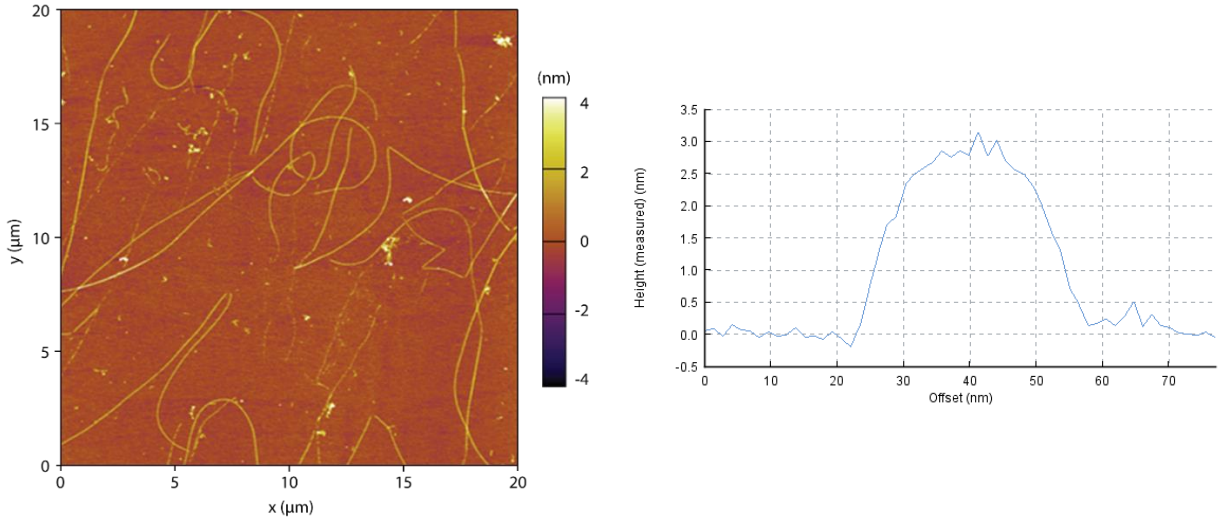

Supplementary Fig. 28. A representative AFM profile of compound **3** nanoribbons deposited on mica illustrates nanoribbon lengths up to 20 µm as determined by ImageJ analysis. A sample nanoribbon height profile is shown. AFM nanoribbon cross-section analysis reveals heights of 3.7 ± 0.5 nm (average over height measurements of 61 nanoribbons). Nanoribbon widths are not extracted from AFM due to tip convolution.

S3e. Scanning electron microscopy

Cast Films

We observed the hierarchical structure of AA threads by SEM (Supplementary Fig. 30). Striations along the thread axis of the dried threads are consistent with long-range alignment of nanoribbon bundles resulting from the shear alignment process.

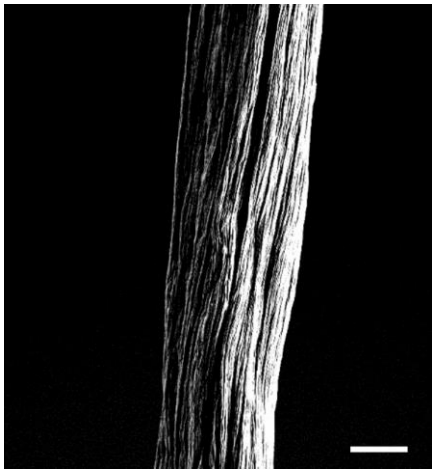

Supplementary Fig. 29. SEM of a 20 μm-diameter nanoribbon thread shows long-range alignment of nanoribbon bundles (scale bar, 10 μm).

S3f. Förster resonance energy transfer

EDANS and DABCYL serve as a typical Förster resonance energy transfer (FRET) pair with a Förster radius of 3.3 nm[39]. When the donor and quencher approach the Förster radius, energy transfer from the donor to the quencher results in a reduction of fluorescence intensity through vibrational relaxation pathways. Therefore, decreases in fluorescence intensity correlate to molecular exchange between adjacent nanoribbons (Figure 2D-E).

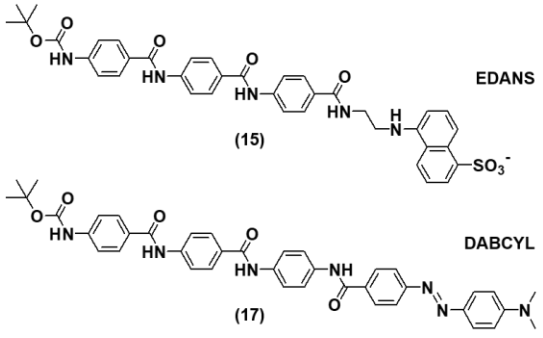

Supplementary Fig. 30. EDANS and DABCYL-based aramid amphiphiles used in the FRET study.

As a control, completely mixed co-assemblies of amphiphiles labeled with both a donor fluorophore and dark quencher show a 76% reduction in fluorescence intensity relative to assemblies labeled solely with the fluorophore (Supplementary Fig. 31).

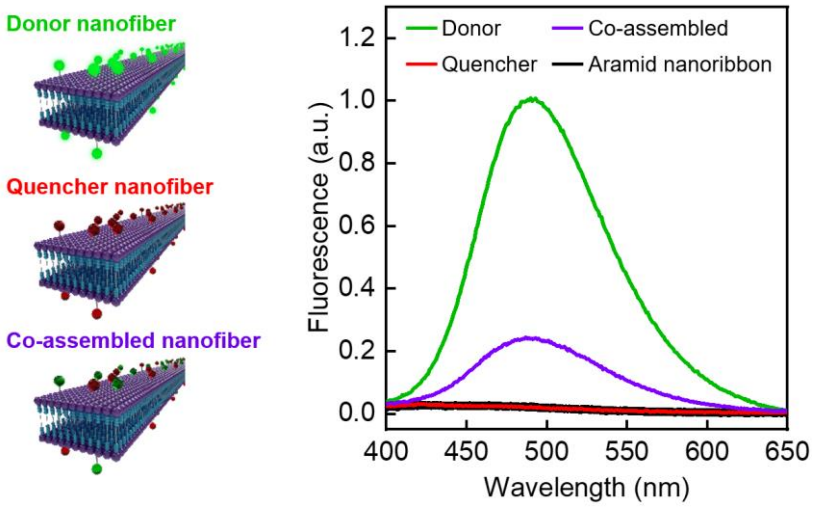

Supplementary Fig. S31. The fluorescence intensity of nanoribbons labeled with the FRET donor EDANS is quenched by 76% when co-assembled with FRET quencher DABCYL.

S3g. Stiffness determination by topographical analysis of nanoribbon contours

Sample preparation: Compound **3** was chosen for analysis by atomic force microscopy (AFM) because of its high solubility and favorable surface interaction with AFM substrates. DI water was added to a lyophilized sample of **3** to reach 30 mg/mL. A sonicator bath was used to accelerate self-assembly. After 24 h at room temperature, the suspension was diluted to 0.03 mg/mL and deposited on a clean glass surface. The glass substrate was prepared through cleanings with DI H_2O and ethanol, drying with stream of N_2 (g), and activation by UV/ozone treatment. After 5 min of incubating the nanoribbon suspension on the clean glass, the surface was rinsed with DI water and used directly for AFM imaging.

Experimental details: AFM images (Supplementary Fig. 32) were used to determine the persistence length and Young's modulus of the ribbons. Fluctuations of ribbon shape are statistically processed using the Easyworm software tool[43], which traces parametric splines to the contours of many ribbons of the same sample (in this experiment, n = 29 ribbons). Parametric splines store the $x - y$ coordinates of all the knots along the ribbons. Each combination of two knots gives a secant length L, and the midpoint of this secant deviates from the ribbon contour by a distance δ. The persistence length P is then obtained by least-square fitting the data to the worm-like chain model for semi-flexible polymers, $< \delta^2 > = L^3/(48 \times P)$, for ribbons equilibrating in 2-D. The persistence length reflects how much a ribbon bends as a result of thermal fluctuations. A higher persistence length of a ribbon corresponds to a lesser change in orientation over a given distance along its contour. The flexural rigidity F is the result of scaling the persistence length to the thermal energy according to $F = P \times k_B T$. Finally, the Young's (elastic) modulus E is obtained using $E = F/I$, where I is the area moment of inertia, which reflects the resistance to bending of a cross-section. For the circular cross-section observed in AFM measurements, the moment of inertia, $I = \pi \cdot d^4/64$, where d is the ribbon diameter. Heights of each nanoribbon were estimated by analysis of nanoribbon cross-sections observed in the AFM images. The AFM height measurements are consistent with cryo-TEM and SAXS measurements, and therefore we use $d = 3.7 \pm 0.5$ nm to calculate I.

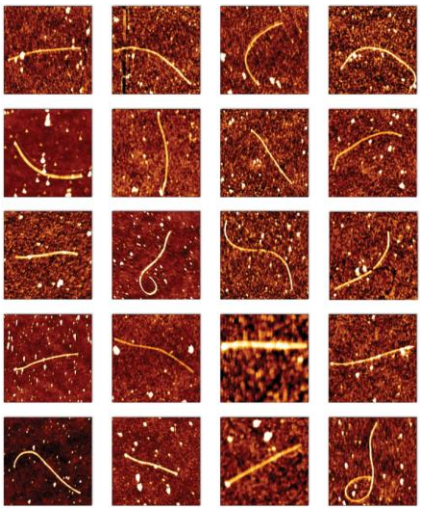

Supplementary Fig. 32. Contour traces of AFM images of AA nanoribbons, a representative set of which are shown here, were used for determining nanoribbon stiffness by statistical topographical analysis. Image dimensions are 1 μm x 1 μm.

S3h. Yield strength determination by sonication-induced scission

We measure the yield (tensile) strength σ* by using a sonication-induced fibril scission technique, as detailed in our previous work[48]. In short, sonication creates collapsing cavitation bubbles, causing fluid velocity fields to trap fibrils and exert shear forces on them. This leads to fibril extension in opposite directions and mechanically-induced rupture at the site of highest stress. The model developed by Huang et al. implies that the forces exerted on the fibril decrease dramatically with the fibril length[44]. Hence there is a threshold length L_{lim} below which a fibril of a given cross-section will not break anymore. We plot the length of hundreds of fibril fragments as a function of their cross-sectional size (see Supplementary Fig. 33), and derive σ from the relationship[44]:

$$L_{\mathrm{lim}} = \alpha C \sqrt{\sigma} \qquad (1)$$

where $\alpha = 7.10^{-4}$ is a prefactor that depends on the experimental conditions, and C reflects the cross-sectional size of the fibril fragments. For a rectangular cross-section fibril with long edge w (i.e. TEM width), and short edge h (i.e. AFM height), it is given by[48]:

$$C = \left[\frac{\gamma}{2w^2}\left[\left(\ln\left(\gamma + \sqrt{\gamma^2 + 1}\right) + \ln(\gamma^{-1} + \sqrt{\gamma^{-2} + 1})\right]\right]^{-1/2} \qquad (2)$$

where $\gamma = w/h$ is the aspect ratio. After prolonged sonication time, fibril length distribution reaches a plateau and the size of fragments that belong to a sample fall in a "terminal range" defined by $\left[{L_{lim}}/{2}, L_{\mathrm{lim}}\right]$. However, we expect an even broader distribution of fragment lengths L, because both the cross-sectional area and intrinsic strength can vary. This broadening of the terminal range is considered by determining the lines of best fit from the extremities of the distribution[48]. We represent the extremities by the 5–10 data points corresponding to the smallest and longest aspect ratios L/C (see the black dots in Supplementary Fig. 34), discarding obvious outliers. The lowest slope s reflects the low boundary of the shortest terminal range (*i.e.* the smallest aspect ratio), and the highest slope S exposes the high boundary of the longest terminal range (*i.e.* the longest aspect ratio). The shortest and longest terminal ranges are thus defined by intervals $[s, 2s]$ and $[S/2, S]$, respectively. L_{lim} is the averaged top of any terminal range given by:

$$\frac{L_{\mathrm{lim}}}{C} = \frac{2s + S}{2} \pm \frac{2s - S}{2} \qquad (3)$$

Combining the results of Eq. 2 with Eq. 1 we obtain the tensile strength σ. This method is particularly solid to reveal at least the position of the lower edge of the terminal distribution, which corresponds to the lowest possible strength of the fibril sample. Using the absolute error ± (2s – S)/2 provides a simple way to account both for any experimental source of error and for the strength variability within a given sample. In this study all fibril fragments have a similar cross-sectional area, with w = 6.0 ± 1.3 nm and h = 3.1 ± 0.5 nm. Consequently, most fragment lengths are distributed in one single terminal range $\left[\frac{L_{\mathrm{lim}}}{2}, L_{\mathrm{lim}}\right]$, as displayed in the histogram of the fragment length distribution (see Supplementary Fig. 33). In order not to overestimate the strength, we use a cut-off value to discard all fibril fragments with L > 134 nm. These fragments most likely escaped sonication-induced breakage because the initial fibril concentration was relatively high (~0.5 mg/mL); as a result, their lengths did not end up into the terminal range. To calculate the cut-off, we assume the most prominent peak of the distribution to correspond to $L_{\mathrm{lim}}/2$ and fit a Gaussian to that peak, which gives $L_{\mathrm{lim}}/2$ = 55 ± 12 nm for TEM. We thence estimate L_{lim} = 110 ± 24 for TEM and use it to derive the cut-off.

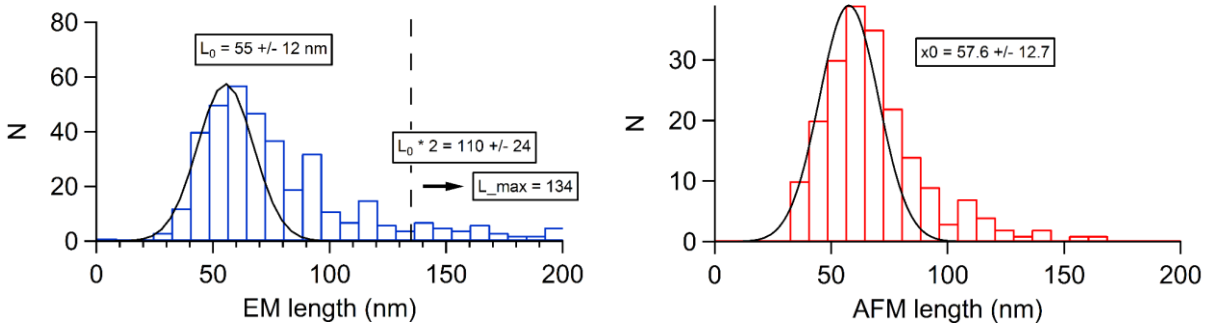

Supplementary Fig. 33. The distribution of fragment lengths after sonication-induced scission of nanoribbons of **3** as measured by (**A**) TEM and (**B**) AFM.

Here the fragment lengths were independently estimated in both TEM and AFM measurements. Both techniques give similar results, also translating in similar strength values. For the determination of the cross-sectional parameter C, we used the AFM-determined mean height of the fibril fragments $h = 1.96 \pm 0.55$ nm in the analysis of the TEM data (Supplementary Fig. 33a), and we used the TEM-determined mean width of the fibril fragments $w = 6.0 \pm 1.3$ nm in the analysis of the AFM data (Supplementary Fig. 33b). Note that the mean AFM height of the fibril fragments is lower than that of non-sonicated fibrils, possibly because non-sonicated fibrils are higher-order assemblies and sonication leads to partial disassembly of the several protofilaments that form a "mature" fibril. The highest and lowest lines in this plot identify L_{lim} and the smallest fragments produced by sonication, respectively, and the yellow region considers a broadening of these bounds due to variations in cross-sectional area and intrinsic strength.

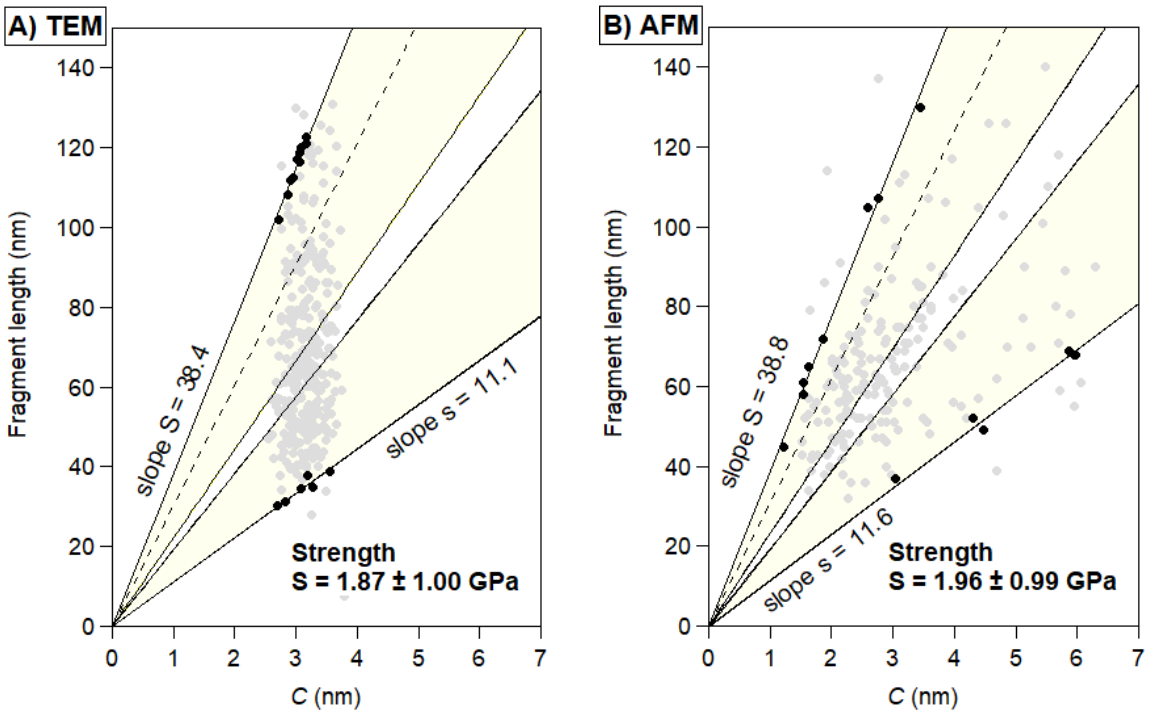

Supplementary Fig. 34. Yield strength analysis of nanoribbons of **3** from sonication-induced scission identifies strengths of (**A**) 1.87 ± 1.00 GPa based on TEM and (**B**) 1.96 ± 0.99 GPa based on AFM analysis of the nanoribbon fragments, showing a close convergence between the two techniques.

S3i. Tensile strength testing of macroscopic AA nanoribbon threads

Tensile testing was performed to obtain Young's modulus and elongation at break values for AA threads formed with sulfate or methanedisulfonate counterions. These results from the mechanical tests are summarized in Supplementary Figs. 35 and 36 below for n = 6 threads per counterion.

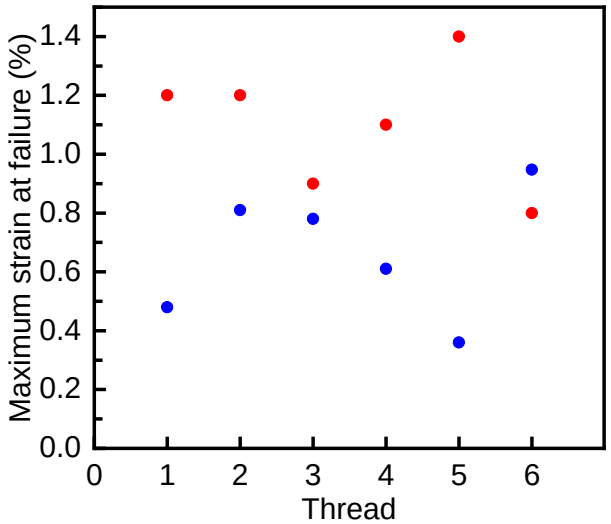

Supplementary Fig. 35. The Young's elastic modulus for sulfate (blue) and methanedisulfonate (red) AA threads is extracted from their tensile test curves.

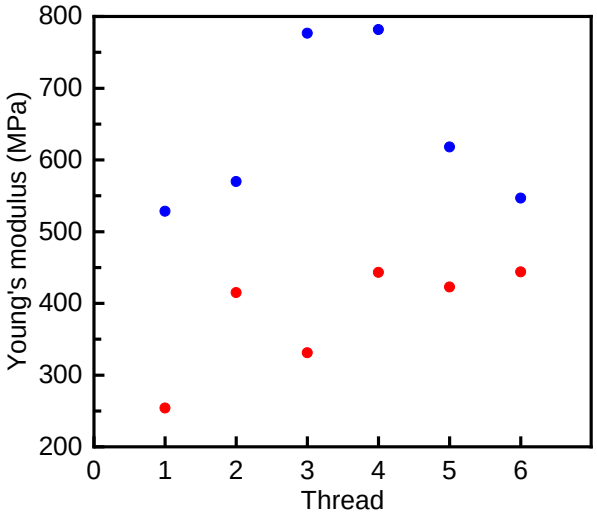

Supplementary Fig. 36. The elongation at break for sulfate (blue) and methanedisulfonate (red) AA threads is extracted from their tensile test curves.